

Lensing in the Blue III: Weak Lensing Shape Catalogs of 30 Merging Galaxy Clusters

SAYAN SAHA ¹, JACQUELINE E. MCCLEARY ¹, SPENCER W. EVERETT ², MAYA AMIT ^{3,1},
GEORGIOS N. VASSILAKIS ^{4,5,6,1}, EMAAD PARACHA ⁷, LEO W.H. FUNG ^{8,9}, STEVEN J. BENTON ¹⁰,
WILLIAM C. JONES ¹⁰, GAVIN LEROY ^{8,9}, ERIC M. HUFF ¹¹, RICHARD MASSEY ^{9,8,12}, THUY VY T. LUU,¹⁰
AJAY S. GILL ¹³, MOHAMED M. SHABAN ^{14,7}, PHILIPPE VOYER ^{10,15}, ANTHONY M. BROWN ^{12,9},
GIULIA CERINI ¹¹, PAUL CLARK ¹², MATTHEW CRAIGIE ¹¹, CHRISTOPHER J. DAMAREN ¹⁶, TIM EIFLER ¹⁷,
DAVID HARVEY ¹⁸, ERIC HABJAN ¹, JOHN W. HARTLEY,¹⁹ BRADLEY HOLDER,¹⁶ MATHILDE JAUZAC ⁸,
DAVID LAGATTUTA ⁸, JASON S.-Y. LEUNG ²⁰, LUN LI ¹⁰, JOHANNA M. NAGY ²¹, C. BARTH NETTERFIELD,^{22,23,7}
SUSAN F. REDMOND ¹¹, JASON D. RHODES ¹¹, ANDREW ROBERTSON ¹¹, L. JAVIER ROMUALDEZ ¹⁹,
JÜRGEN SCHMOLL ⁸, ELLEN SIRKS ²⁴, SUT IENG TAM ²⁵, ANDRÉ Z. VITORELLI ¹¹ AND ALFREDO ZENTENO ²⁶

SUPERBIT COLLABORATION

¹*Department of Physics, Northeastern University*

²*Department of Physics, California Institute of Technology*

³*Center for Data Science, New York University*

⁴*Institute of Astronomy, University of Cambridge*

⁵*Department of Applied Mathematics and Theoretical Physics, University of Cambridge*

⁶*Kaoli Institute for Cosmology, University of Cambridge*

⁷*Department of Physics, University of Toronto*

⁸*Institute for Computational Cosmology, Department of Physics, Durham University*

⁹*Centre for Extragalactic Astronomy, Department of Physics, Durham University*

¹⁰*Department of Physics, Princeton University*

¹¹*Jet Propulsion Laboratory, California Institute of Technology*

¹²*Centre for Advanced Instrumentation (CfAI), Durham University*

¹³*National Research Council Canada Herzberg Astronomy and Astrophysics Research Centre*

¹⁴*Scale AI, Inc.*

¹⁵*Department of Mechanical and Aerospace Engineering, Princeton University*

¹⁶*University of Toronto Institute for Aerospace Studies (UTIAS)*

¹⁷*Department of Astronomy/Steward Observatory, University of Arizona*

¹⁸*Laboratoire d'Astrophysique, EPFL, Observatoire de Sauverny*

¹⁹*StarSpec Technologies Inc.*

²⁰*Imperial College London*

²¹*Department of Physics, Case Western Reserve University*

²²*David A. Dunlap Dept. of Astronomy and Astrophysics, University of Toronto*

²³*Dunlap Institute for Astronomy and Astrophysics, University of Toronto*

²⁴*Departamento de Física Teórica, Universidad Autónoma de Madrid*

²⁵*Institute of Physics, National Yang Ming Chiao Tung University*

²⁶*Cerro Tololo Inter-American Observatory / NSF NOIRLab*

ABSTRACT

We present the weak gravitational lensing dataset from the Super-pressure Balloon-Borne Imaging Telescope (SuperBIT), which imaged 30 galaxy clusters during its 45 night flight in April to May 2023. SuperBIT is a first-of-its-kind balloon-borne imaging telescope that achieved near diffraction-limited observations in near-space conditions above 98% of the Earth's atmosphere. We use the METACALIBRATION algorithm to obtain calibrated galaxy shapes for our target clusters and several calibration fields, enabling unbiased reconstruction of the weak-lensing signal. We employ several diagnostics throughout the pipeline, including assessments of point-spread function (PSF) modeling

residuals and their impact on weak-lensing measurements, as well as tests for correlations between galaxy shapes and measured galaxy and PSF properties. To assess the multiplicative shear bias of the pipeline, we analyze a parallel set of simulated images that incorporate the real observing conditions from the flight, including measured SuperBIT PSFs, observed sky backgrounds, and detector noise, yielding a bias of (1.1 ± 7.8) per cent.

1. INTRODUCTION

Galaxy clusters are the largest gravitationally bound structures in the Universe and provide a powerful probe of cosmology. The abundance of clusters as a function of their mass and redshift offers direct insight into the growth of structure, influencing our understanding of matter density (Ω_m), matter fluctuation amplitude (σ_8), dark energy equation of state, and sum of neutrino masses (A. Vikhlinin et al. 2009; S. W. Allen et al. 2011; A. B. Mantz et al. 2014, 2015). Beyond their cosmological significance, galaxy clusters, particularly merging systems, provide unique laboratories for studying the interplay between dark matter and baryonic components, and can potentially constrain alternative dark-matter models (D. Clowe et al. 2004; A. Robertson et al. 2017; E. L. Sirks et al. 2024).

While galaxy richness (B. P. Koester et al. 2007; S. Andreon 2016), X-ray emission from the hot gas of the intracluster medium (A. Vikhlinin et al. 2009; M. Arnaud et al. 2005), and the Sunyaev–Zeldovich (SZ) effect (K. Vanderlinde et al. 2010; P. A. R. Ade et al. 2016) probe the baryonic component of galaxy clusters, the most direct and least biased probe of their total mass, dominated by dark matter, is weak gravitational lensing of background galaxies. Gravitational lensing refers to the deflection of light from background sources due to the curvature of space-time induced by intervening mass. Such deflections distort the surface brightness profiles of background galaxies. When these distortions are at the level of a few percent or less, the effect is termed *weak* lensing (see M. Bartelmann & P. Schneider 2001 for a review). These distortions can be decomposed into two components: magnification (convergence), which cannot be directly measured, and stretching (shear), which can only be measured statistically by averaging over many galaxies. Measurements of shear can then be used to map the intervening mass distribution (N. Kaiser & G. Squires 1993).

In this work we present the weak-lensing data obtained with the Super-pressure Balloon-borne Imaging Telescope (SuperBIT) (A. S. Gill et al. 2024), which flew from April to May 2023 at an altitude of approximately 33 km, above $\sim 98\%$ of the Earth’s atmosphere. Observing in the stratosphere enables near-space-quality imaging at a fraction of the cost of space missions. During the flight, SuperBIT obtained deep imaging of 30

galaxy clusters, most of which are in merging states, each covering a field of view of approximately $15' \times 23'$.

This work is Paper III in the *Lensing in the Blue* series. Paper I (M. M. Shaaban et al. 2022) describes the unique observing conditions available in the stratosphere and demonstrates that, unlike ground- and space-based missions that are typically optimized for weak-lensing observations at red wavelengths, SuperBIT is particularly well suited for lensing studies in blue wavelengths. Its diffraction-limited optics provide near-perfect transmission between 280 nm and 900 nm, while the stratospheric environment yields exceptionally low sky backgrounds at blue wavelengths (A. S. Gill et al. 2022; M. M. Shaaban et al. 2022). Paper II (J. E. McCleary et al. 2023) introduced the SuperBIT weak-lensing pipeline and the associated simulation framework, and presented forecasts of the achievable lensing signal reconstruction under expected observing conditions. In the present work (Paper III), we analyze the imaging data obtained during the 2023 flight and construct the weak-lensing shape catalog.

Precise measurement of individual galaxy shapes (ellipticities) for weak-lensing science (G. M. Bernstein & M. Jarvis 2002; C. M. Hirata & U. Seljak 2003), particularly in the presence of observational non-idealities, is a highly non-trivial step. Besides, the applied gravitational shear typically induces distortions at only the percent level, whereas intrinsic galaxy ellipticities are an order of magnitude larger and unknown. Consequently, shear can only be inferred through statistical averaging of galaxy shapes under the assumption that the applied shear is locally constant. The intrinsic scatter in galaxy ellipticities produces the so-called *shape noise*, which constitutes the dominant statistical uncertainty in weak-lensing measurements and can only be reduced by increasing the source density.

Since its first detections (D. M. Wittman et al. 2000; D. J. Bacon et al. 2000; N. Kaiser et al. 2000; L. Van Waerbeke et al. 2000), weak gravitational lensing has become a cornerstone of precision cosmology, providing a unique probe of the large-scale structure of the Universe and enabling constraints on structure growth and cosmic evolution (M. Bartelmann & P. Schneider 2001; P. Schneider 2006). Technological advances have led to significant improvements in image depth, resolution, and quality, resulting in higher source densities

and increased statistical power. In parallel, major efforts over the past decade have focused on improving shape-measurement algorithms to extract accurate shear information from faint and distant sources. Modern approaches rely on calibrating measured shapes to infer the applied shear. While early calibration schemes relied heavily on image simulations (C. Heymans et al. 2006; R. Massey et al. 2007; S. Bridle et al. 2010; T. D. Kitching et al. 2012; R. Mandelbaum et al. 2015), more recent methods use empirical calibration directly on observational data, most notably METACALIBRATION (E. Huff & R. Mandelbaum 2017; E. S. Sheldon & E. M. Huff 2017), which naturally accounts for many observational non-idealities. These methods continue to evolve to mitigate increasingly subtle systematic effects relevant for high-resolution data (E. S. Sheldon et al. 2020; X. Li et al. 2022; X. Li & R. Mandelbaum 2023).

In this work, we first describe the SuperBIT data characteristics and preprocessing steps, including image stacking, source detection, and removal of spurious detections. We then present our modeling of the point-spread function (PSF) for individual exposures and evaluate several PSF diagnostics relevant for weak-lensing analyses. We next describe the shape measurement pipeline based on METACALIBRATION algorithm and perform empirical tests of the resulting shape catalogs, including tests for residual PSF–galaxy correlations. Finally, we validate the pipeline using image simulations, including a suite of unit tests incorporating SuperBIT PSFs and fiducial simulations representative of real data, to estimate shear bias and PSF ellipticity leakage.

The paper is organized as follows. Section 2 provides an overview of the data and preprocessing steps. Section 3 describes PSF modeling and associated diagnostics. Section 4 presents the METACALIBRATION implementation and empirical tests of the resulting shape catalogs. Section 5 describes the simulation framework used to validate the pipeline. Finally, Section 6 summarizes the results and provides an outlook for future work.

2. DATA

2.1. Instrument & Flight Overview

SuperBIT employed a modified Dall-Kirkham telescope, with a 0.5 m primary mirror and a three-lens corrector to obtain near-diffraction-limited imaging from the stratosphere, across a $\sim 0.1 \text{ deg}^2$ field of view (A. S. Gill et al. 2024). Flying at an altitude of nearly 33 km on NASA’s Super-pressure balloon, SuperBIT operated above 98% of Earth’s atmosphere. During its 2023 long-duration flight, launched from Wānaka, New Zealand on

April 16, 2023, SuperBIT circumnavigated the Southern Hemisphere five times over 45 nights, taking multi-band images of more than 30 galaxy clusters for weak lensing analysis.

SuperBIT’s optical assembly was mounted on a lightweight aluminum honeycomb gondola with nested gimbal frames providing three-axis stabilization and control in yaw, pitch, and roll. This design helped isolate the telescope’s line-of-sight from balloon-induced compound pendulations while compensating for sky rotation to maintain stable pointing for up to several hours (L. J. Romualdez et al. 2020). Telescope stabilization was guided by inertial gyroscopes and two wide-field star cameras that matched observed stars to catalogs using `astrometry.net` (D. Lang et al. 2010).

Additional tip-tilt image stabilization was achieved by using a high-speed fine-steering mirror guided by two focal-plane star cameras (P. Voyer et al. 2024). These systems collectively achieved a telescope pointing stability of $0.34''$ and a focal-plane image stability of $0.055''$ over (multiple) 5 minute exposures (A. S. Gill et al. 2024).

SuperBIT’s images were taken with a QHY600M science camera using a Sony IMX-455 CMOS sensor (9576×6388 pixels, $3.76 \mu\text{m}$ per pixel) with low read noise, high quantum efficiency, and a pixel scale of $0.144''/\text{pixel}$. Observations were primarily conducted in three filters: F400W (307–434 nm), F480W (366–575 nm), and F600W (518–702 nm), corresponding to ultraviolet, blue, and green bands, respectively. These bands were chosen for the small diffraction limit and high throughput of the system in those wavelengths, and consequent ability to measure the shapes of faint galaxies (J. E. McCleary et al. 2023).

The SuperBIT gondola had six lithium-iron-phosphate batteries (11 kWh total) charged by solar panels, along with heaters and insulation to maintain stable temperatures while the gondola went through significant day/night swings (from $+50^\circ\text{C}$ to -60°C) (A. S. Gill et al. 2024). Data and telemetry were down-linked using Iridium, Pilot, NASA’s TDRSS links, and SpaceX’s Starlink (E. Paracha et al. 2024), with additional physical droppable 5TB storage systems for redundancy, ensuring all science data could be retrieved (E. L. Sirks et al. 2020).

SuperBIT’s sub-arcsecond stability allowed it to take near-diffraction-limited images with space-like quality, which was well suited to conduct the weak-lensing shape measurements presented in this paper.

2.2. Image Pre-processing

We acquired dedicated dark frames prior to sunrise on every flight day and constructed master darks of each exposure time planned for science observations. SuperBIT’s main science camera did not use a shutter, so, to prevent sky and sunlight contamination, we kept only the frames that were acquired at sun elevations $< -6.5^\circ$. To construct the master dark for each exposure time, we checked the pixel value distributions for each dark. Because histograms showed a narrow Gaussian core with a pronounced positive tail of hot pixels, a simple σ -clipping would have produced a biased mean dark current. Instead, we defined lower/upper inclusion thresholds (“haircuts”) at the departure from Gaussianity and classified pixels outside of the boundaries as cold/hot, which were then used to create the master dark images and bad pixel masks.

We then averaged values *per pixel* over the focal plane to generate master darks, but only included pixel samples in the haircut for each exposure time. To be sensitive to temporal effects, a pixel in the final master was kept if it was in the “haircut” in $> 55\%$ of the total dark images. The threshold was chosen as an optimal trade-off: big enough to down-weight pixels experiencing intermittently high dark current or long-term deterioration, but small or permissive enough to keep otherwise stable pixels that sometimes scattered or had high dark current due to random cosmic rays. Using this cut, the percentage of pixels lost to haircutting was $< 2\%$ across the focal plane with a clean, low-noise master dark. In master dark, pixels with no “good” contributors were in-filled with a computed median-stack dark for continuity.

For scientific frames, we first extracted and smoothed cosmic rays with L.A.Cosmic (P. G. van Dokkum 2001) and subtracted the corresponding exposure-time master dark to remove bias structure and dark current before obtaining “cleaned” science images for astrometric and photometric processing. Hot pixels were identified in the master dark creation process described above, and were flagged separately for treatment in subsequent processing. With these “clean images”, we were able to suppress and account for the long-tailed hot-pixel population without distorting the Gaussian core in the distribution, achieving spatially smooth residual backgrounds for stable photometric calibration of SuperBIT’s scientific frames.

2.3. Targets and Observation Footprint

The primary scientific goal of the SuperBIT mission was to constrain the self-interaction cross-section of dark matter using relative positions of the dark matter, in-

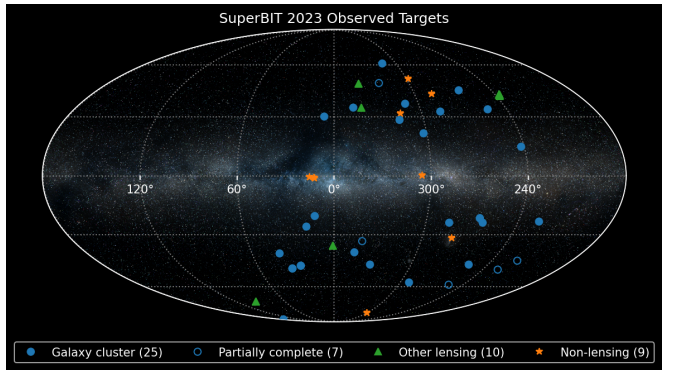


Figure 1. On-sky distribution of SuperBIT observations, including galaxy clusters and non-lensing targets.

tracluster medium (ICM) and stars, during mergers between galaxy clusters. The technique works as follows. As two galaxy clusters collide, the stars in member galaxies are effectively collisionless, experiencing only gravitational interactions as they pass by one another. By contrast, the ICM is highly collisional, with ram pressure slowing the two clouds of (mainly hydrogen) gas, which lag behind and become spatially offset from the galaxies (D. Clowe et al. 2004). The location and spatial distribution of the dark matter—which can be probed via gravitational lensing—relative to the ICM and galaxies will depend on the degree of its self-interaction: in the cold dark matter paradigm, dark matter particles are collisionless and so should be entirely coincident with the stellar component. If the dark matter is self-interacting (SIDM), the merging dark matter halos will experience a mild net deceleration, leading to small spatial offsets from the galaxy distribution (S. W. Randall et al. 2008; A. Robertson et al. 2017). Under certain assumptions, the relative spatial offsets of the dark matter, ICM, and galaxies can then be translated to a measurement of the cross-section for non-gravitational interactions between two dark matter particles, σ/m (D. Harvey et al. 2015, 2017; D. Wittman et al. 2018; E. L. Sirks et al. 2024). It is easiest to resolve physical separations if the cluster is nearby, but the nearest clusters are inefficient gravitational lenses, and their shear signal is diluted over a large area. For observations with as large a field of view as SuperBIT, the sensitivity of this experiment is optimal at redshift $0.05 \lesssim z \lesssim 0.3$ (R. Massey et al. 2011).

Accordingly, SuperBIT’s primary targets comprised a set of massive galaxy clusters, observable from Southern mid-latitudes and with dual peaks in X-ray or thermal Sunyaev-Zel’dovich (tSZ) signals, or known to be clusters merging in a direction close to the plane of the sky from e.g. radio shock fronts. Target clusters were chosen to have abundant ancillary data: deep tSZ and

X-ray imaging for mapping the ICM and, ideally, Hubble Space Telescope imaging for strong lensing studies of the cluster cores. Several targets also appear in the Local Volume Complete Cluster Survey (LoVoCCS, S. Fu et al. 2024), the Dark Energy Spectroscopic Instrument Data Release 1 (DESI Collaboration et al. 2025), and the Dark Energy Survey (A. Zenteno et al. 2020; J. Prat et al. 2022).

Informed by the forecasts of M. M. Shaaban et al. (2022) and J. E. McCleary et al. (2023), the survey strategy consisted of three hours per cluster in F400W and F480W plus 90 minutes in F600W. Template galaxy spectra at redshifts $0 < z_{\text{gal}} < 1.5$ showed that cuts in this color-color space could separate foreground and background galaxies of most spectral types from those in a fiducial $z = 0.5$ cluster.

Based on these criteria, we compiled and ranked a list of ~ 100 viable clusters. An autonomous “autopi- lot” algorithm on the payload then selected targets from among the list, based on scientific rank as well as target visibility, guide star magnitude, the number of exposures per band of the target already taken, and the previous history of image quality (A. S. Gill et al. 2024). When the mission was terminated, SuperBIT had obtained complete or near-complete observations for 30 merging galaxy clusters at $0.01 < z < 1$ (Figure 1). Partial data exists for another ten clusters. Six pointings within the COSMOS field were also obtained for calibration of weak lensing shears (A. Leauthaud et al. 2007) and photometry (N. Scoville et al. 2007; C. M. Casey et al. 2023). Completed cluster observations and calibration fields are presented in Table 2.

2.4. Astrometry

As is standard practice, SuperBIT exposures were astrometrically calibrated by matching image sources to a reference catalog and fitting field distortions. To perform these fits, we used the `solve-field` command from `astrometry.net` (D. Lang et al. 2010) after stripping any pre-existing WCS keywords from the FITS headers. Given the frame size, we restricted solutions to the small-field-of-view 5200-series index files built from Tycho-2 and *Gaia* DR2. In practice, 98% of fields were solved with index 5202 and the remaining 2% with index 5200. We removed the larger-scale 5203–5206 indices from `astrometry.net`’s available dataset because their quad diameters are comparable to a substantial fraction of a SuperBIT frame, reducing the density of fully contained asterisms and yielding less robust WCS matches across the entire field-of-view. In particular, quads 5205–5206 approach the entire frame width, whereas quads 5203–5204 are intermediate and were omitted to

maximize contained-quad density, reduce spurious hypotheses, and improve overall WCS solutions across the wide field of view. The resulting TAN–SIP solutions were then converted to TAN–TPV for compatibility with SWARP, preserving the polynomial distortion content. Visual overlays against catalogued sources confirmed accurate source placements across the field. The scripts implementing this workflow are publicly available.²⁷

2.5. Stacking and Source Detection

After performing dark subtraction, flat-field correction, and astrometric calibration, the exposures were visually inspected to identify and exclude frames affected by artifacts such as satellite glints, aurora, or other transient anomalies. The resulting “clean” exposures constitute the final set used as input for our shape-measurement pipeline.

The first step of the pipeline involves stacking these clean single exposures to produce a deep coadded image, which serves as the basis for source detection. During the inspection of individual exposures, we identified hot pixels distributed across the CCD plane. These pixels are masked using pre-determined hot-pixel maps, which are applied consistently throughout the pipeline. An example of hot pixels in a single exposure, along with their corresponding masks, is shown in the left panel of Figure 2.

Clean single exposures are stacked using the SWARP algorithm²⁸ (E. Bertin 2010a). For each exposure, we construct weight maps that assign a value of 1 to valid pixels and 0 to hot pixels, while carefully incorporating the WCS information. These weight maps ensure proper pixel weighting during stacking; because dithering prevents hot pixels from aligning across exposures, the weighting effectively mitigates their impact on the coadded image.

While the primary science observations were obtained in the F400W, F480W, and F600W filters (corresponding to the *u*, *b*, and *g* bands), the F480W (*b*-band) images serve as our primary detection band. The header information from the F480W coadd is used to construct the coadds for the F400W and F600W bands, ensuring consistent astrometry across all filters. Sources in the coadds are detected using SEXTRACTOR²⁹ (E. Bertin & S. Arnouts 1996a). Various configuration settings were tested to optimize source detection. The exposure weight maps are provided to SEXTRACTOR to nor-

²⁷ https://github.com/GeorgeVassilakis/wcs_beheader

²⁸ <https://www.astromatic.net/software/swarp/>

²⁹ <https://www.astromatic.net/software/sextractor/>

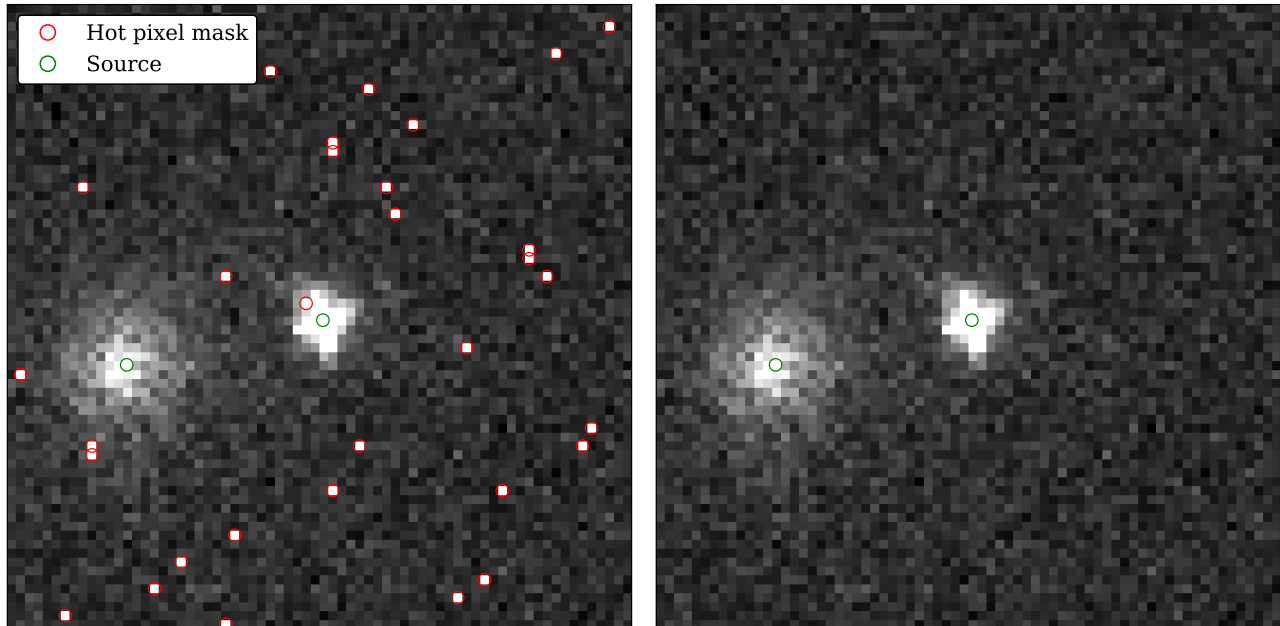


Figure 2. Illustration of the hot-pixel mask implementation in our pipeline. *Left panel:* Example crop of a clean single exposure showing hot pixels (red circles) identified by the pixel mask. Nearby genuine source detections are indicated by green circles. *Right panel:* Background-subtracted image of the same crop, as output by SExtractor when the hot-pixel mask is provided as an input weight/mask map during source extraction. These background-subtracted images are used in subsequent stages of the pipeline for Bayesian shape measurement with NGMIX (detailed in Section 4 and Appendix B). The hot-pixel masks are also supplied during shape fitting, ensuring that the inference is independent of those pixels.

malize flux measurements, ensuring that photometry is independent of the number of exposures contributing to each object. Source detection is performed in the F480W (b) band, while photometric measurements in the F400W (u) and F600W (g) bands are obtained using the dual-image mode of SExtractor applied to the registered coadds generated with SWARP as described above. We also perform source extraction at the single-exposure level, as we need to identify stars required for PSF modeling (see Section 3). In SExtractor, we use the same binary weight maps (ones and zeros) constructed from our hot-pixel masks as used in SWARP. This procedure produces background-subtracted images in which hot pixels are effectively inpainted. An example of such a background-subtracted image, where the hot pixels have been inpainted, is shown in the right panel of Figure 2. We use these background-subtracted images as inputs for Bayesian shape measurement with NGMIX, as detailed in Section 4 and Appendix B. In addition, the hot-pixel mask is supplied to NGMIX during model fitting, ensuring that the inferred galaxy properties are independent of the masked pixels.

After obtaining the detection catalog with SExtractor, we identified spurious detections around diffraction spikes of very bright stars in the field of view, as well as near the edges of exposures. Some of our cluster targets

contain exceptionally bright brightest cluster galaxies (BCGs), which produce similar artifacts. We found that applying selection cuts based on photometric or shape measurement parameters (discussed in Section 4.2) results in the loss of a significant number of valid sources. Therefore, the most efficient approach, without sacrificing true sources, is to apply masks around bright objects.

For this purpose, we manually create polygonal region files around bright sources using the astronomical visualization software SAOImage DS9³⁰ (W. A. Joye & E. Mandel 2003). These region files are generated for all valid targets processed through our pipeline. Sources falling within these masked regions are excluded, while the remaining objects are retained for further analysis. An example of applying such a masking technique to exclude spurious detections around bright sources for the cluster Abell 3411 is shown in Figure 3.

2.6. Photometric Calibration

To photometrically calibrate the coadded science images and determine the zeropoints for each filter, we cross-matched high signal-to-noise stars detected in the SuperBIT images with public photometric catalogs, in-

³⁰ <https://sites.google.com/cfa.harvard.edu/saomageds9>

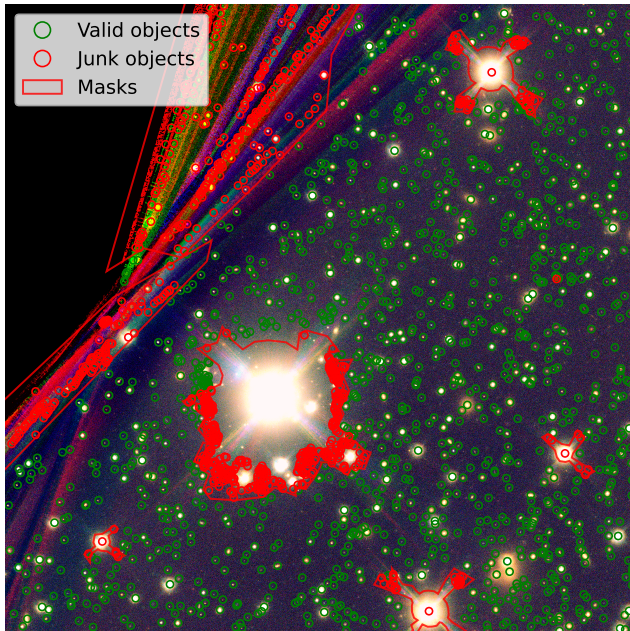


Figure 3. Example of a star-mask applied to the detection catalog on the coadded image. Sources within the masked regions (red) are excluded, while the remaining sources (green) are retained and propagated through the pipeline.

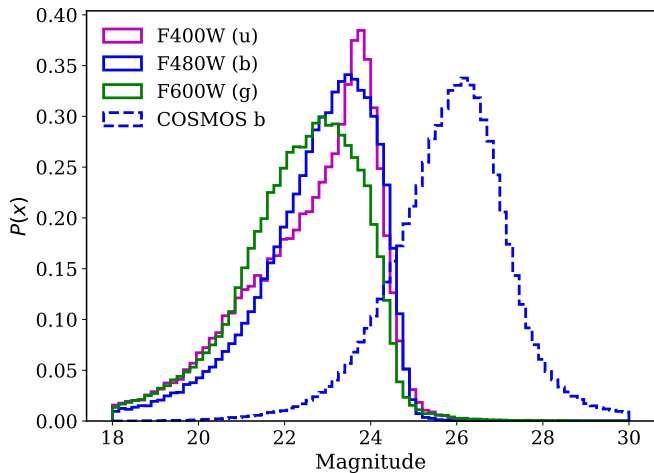


Figure 4. Magnitude distributions in the SuperBIT science filters. The F480W (*b*), F600W (*g*), and F400W (*u*) distributions are shown in blue, green, and magenta, respectively. The dashed blue histogram shows the magnitude distribution of all COSMOS catalog objects as they would be observed through the SuperBIT F480W (*b*) filter. The COSMOS catalog is used to sample galaxy properties in the simulations.

cluding Gaia DR2 (Gaia Collaboration et al. 2016; Gaia Collaboration 2018), Pan-STARRS DR2³¹ (K. C.

³¹ <https://catalogs.mast.stsci.edu/panstarrs/>

Table 1. Photometric zeropoints (ZP) for each SuperBIT filter.

Filter	ZP
F400W (<i>u</i>)	27.148 ± 1.072
F480W (<i>b</i>)	29.146 ± 1.190
F600W (<i>g</i>)	29.391 ± 0.864

Chambers et al. 2016; H. A. Flewelling et al. 2020), and Hyper Suprime-Cam (HSC) DR3 (H. Aihara et al. 2022). We find consistent zeropoint estimates across these catalogs for all bands considered except the UV, which is not covered by the above surveys. To obtain a UV band zeropoint, we therefore implemented a synthetic photometric calibration using Gaia BP/RP spectra, which is in a Vega magnitude system. We integrated matched Gaia spectra with the throughput curves of all SuperBIT filters and computed the corresponding magnitudes. Uncertainties were calculated from the variations of the matched sources and are significant due to the small size of the matched spectra dataset. The zeropoints from the synthetic photometry calibration (Table 1) agree well with the result of the initial standard photometry calibration. To verify the method, we ran the same code on spectra of matched sources with Gaia imaging filters and compared magnitudes from Gaia’s photometry catalog, and the results matched well. The magnitude distributions of detected objects in all three bands are shown in Figure 4.

3. PSF MODELING

The point-spread function (PSF) describes the response of an imaging system to a point source, i.e., how the image of a distant star appears when recorded by the telescope. Accurate modeling of the PSF is essential for weak-lensing analyses because galaxy shapes must be inferred prior to convolution with the PSF (the *pre-PSF* galaxy properties). In practice, the PSF is characterized using stars within the field of view (FOV) of each exposure, which provide localized measurements of the PSF at their respective positions. Since the PSF can vary significantly across the CCD plane, the aim is to model these spatial variations to ensure accurate characterization of the PSF.

3.1. Selection of Stars

Accurate PSF modeling requires selecting stars that reliably represent the PSF. After detecting objects in an exposure, we identify stars by locating the stellar locus in the size–magnitude diagram (using F480W (*b*)-band magnitudes). This identification is aided by cross-matching the detected sources with the *Gaia* DR3 (Gaia

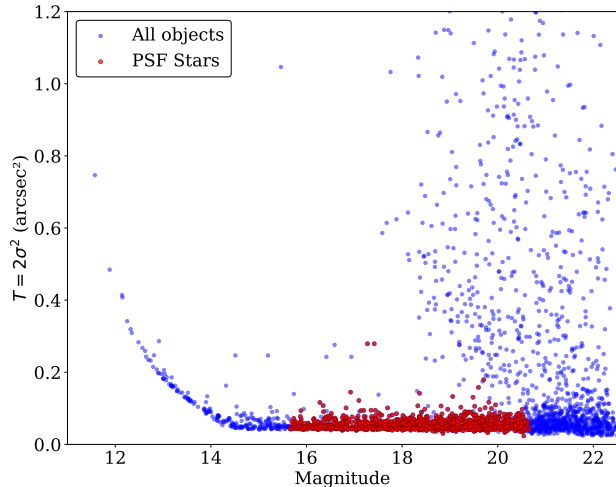


Figure 5. Size–magnitude diagram for a single exposure. The stellar locus is visible, allowing the identification of stars suitable for PSF modeling.

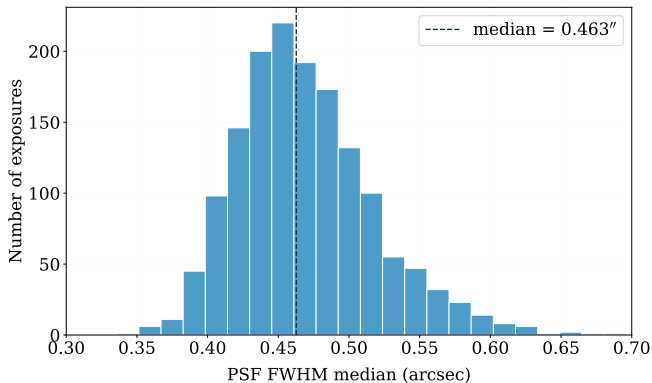


Figure 6. Distribution of median PSF FWHM per exposure. This summarizes image quality across the dataset.

Collaboration et al. 2016, 2023) star catalog, an example of which is shown in Figure 5. The size T and ellipticities e_1 and e_2 are derived from the second-order moments of the light profile, $I(x, y)$ (P. Schneider & C. Seitz 1995):

$$T = Q_{xx} + Q_{yy}, \quad (1)$$

$$e = e_1 + ie_2 = \frac{Q_{xx} - Q_{yy} + 2iQ_{xy}}{Q_{xx} + Q_{yy} + 2\sqrt{Q_{xx}Q_{yy} - Q_{xy}^2}}, \quad (2)$$

where the second-order moments $Q_{\mu\nu}$ are defined as

$$Q_{\mu\nu} = \frac{\int dx dy I(x, y)(\mu - \bar{\mu})(\nu - \bar{\nu})}{\int dx dy I(x, y)}. \quad (3)$$

The moments Q_{ij} are measured using the `AdaptiveMom` method implemented in the `HSM` module (R. Mandelbaum et al. 2005). As shown in Figure 5, the stellar locus is identified by the fact that the size of stars should

be independent of their magnitude. However, for very bright stars, CCD saturation occurs, leading to charge overflow. This effect artificially increases the observed size of the stars, producing what are known as saturated stars. On the other hand, galaxies can have a wide range of sizes, typically larger than the PSF, as illustrated in the figure.

To select stars suitable for PSF modeling, we choose those that are at least 1.5 magnitudes fainter than the faintest saturated stars. We further exclude objects in regions where the stellar locus merges with galaxies by imposing a minimum detection SNR (`SNR_WIN` from `SEXTRACTOR`) of 20. Consequently, the magnitude range of good stars typically lies between $\text{mag} \sim 15.7$ and $\text{mag} \sim 20.5$. We also note that the quality of exposures varies, as reflected in the distribution of stellar sizes (measured via adaptive moments) across exposures. The median FWHM of the selected good stars serves as a useful proxy for assessing exposure quality. Figure 6 shows the distribution of median PSF FWHM for different exposures. The scatter of the stellar locus and the PSF ellipticity across the CCD also serve as useful proxies for exposure quality in the context of shape measurements. We therefore adopt a combined scatter–ellipticity exposure–quality criterion to select exposures used in the shape-measurement pipeline. The exposure selection scheme is described in detail in Appendix A. Another important factor is the number of available good stars for PSF fitting. As discussed in the next section, this number can significantly impact the quality of PSF model interpolation. In our observations, which span a wide range of sky positions, the number of stars per exposure varies as expected: fields near the Galactic plane contain more stars, while high-latitude fields contain fewer. The distribution of the number of stars per exposure across different targets is shown in Figure 7.

3.2. PSF Interpolation & Diagnostics

Stars can be used to trace the spatial variation of the PSF across the field of view. Interpolation is required in regions where no stars are available, particularly at the positions of galaxies, whose intrinsic (pre-PSF) shapes we wish to measure. It is therefore essential to test the PSF model interpolation and to quantify any residuals. We use the `PSFEX`³² (E. Bertin 2011) software to model the PSF on a pixel basis. We have tested several `PSFEX` configuration setups and found that the following configuration yields the lowest modeling residuals:

³² <https://www.astromatic.net/software/psfex/>

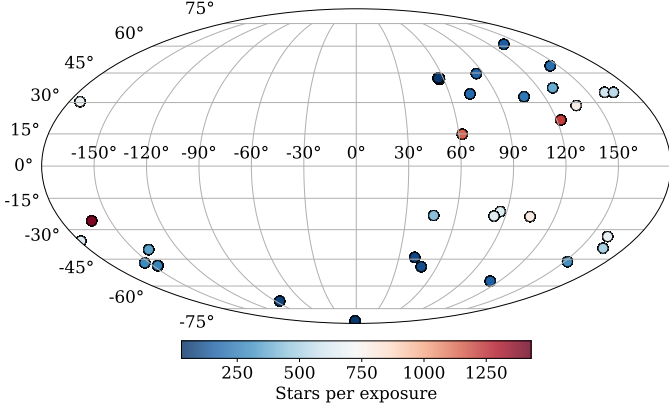


Figure 7. Median number of stars per exposure for each target, shown in Galactic coordinates. Targets near the Galactic plane exhibit significantly higher stellar densities.

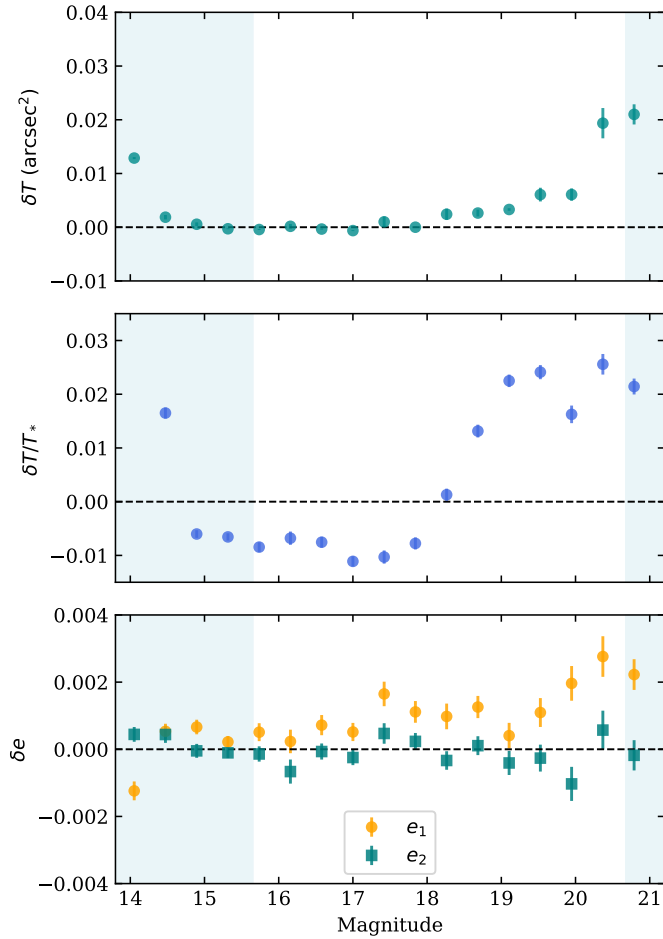


Figure 8. PSF model residuals for the reserved test sample as a function of magnitude: size (top), fractional size (middle), and ellipticity components (bottom). The shaded region indicates stars that were excluded from the PSFEx model fitting. The test sample includes the 20% of good stars reserved for validation, as well as the excluded (bad) stars.

```

BASIS_TYPE PIXEL
PSF_SAMPLING 0.5
PSF_SIZE 101,101
PSFVAR_KEYS XWIN_IMAGE,YWIN_IMAGE
PSFVAR_GROUPS 1,1
PSFVAR_DEGREES 5
    
```

For each exposure, the good stars selected in the previous subsection are randomly split into training and validation samples in an 80:20 ratio. The PSF model is fitted on the 80% training set, while the remaining 20% are reserved to assess the accuracy of the interpolation.

After fitting the model with the PSFEx settings described above, we evaluate the PSF at the positions of the test stars. For both the observed star images and the PSF model renderings, we measure the sizes and ellipticities using the second-order adaptive moments defined in Eq. 1 and Eq. 2. This procedure is carried out for all exposures across all targets. Figure 8 presents the model residuals in size and ellipticity as a function of magnitude. Importantly, the validation sample includes both the 20% of reserved good stars and the stars excluded by our selection criteria, i.e., those that are either saturated (very bright) or have very low detection SNR. The shaded regions in Figure 8 denote the magnitude ranges excluded from the training sample.

We further assess the spatial variability of the PSF interpolation quality in CCD coordinates, shown in Figure 9, where we compare the measured ellipticity and size of the test stars with the PSFEx model predictions and display the corresponding residuals across the detector.

In principle, PSF modeling residuals can propagate into galaxy shape measurements and subsequently bias the reconstruction of the weak-lensing signal. A standard way to quantify this effect is to inspect the contribution of PSF model residuals to the two-point shear correlation statistics (M. Jarvis et al. 2003, 2016), defined as

$$\xi_+(\theta) = \langle e(\mathbf{x})e(\mathbf{x} + \theta) \rangle. \quad (4)$$

Although our aim is to measure the true shear from an ensemble of galaxies, all shape measurement algorithms are subject to systematic biases. A common parametrization (C. Heymans et al. 2006) is

$$\langle e \rangle = (1 + m)g_{\text{true}} + \alpha e_{\text{PSF}} + c, \quad (5)$$

where m represents the multiplicative bias, α quantifies the “leakage” of PSF shape e_{PSF} into galaxy shapes, and c denotes an additive bias. With this parametrization, the contribution of PSF leakage to the shear two-point function in Eq.4 can be expressed as (M. Jarvis et al.

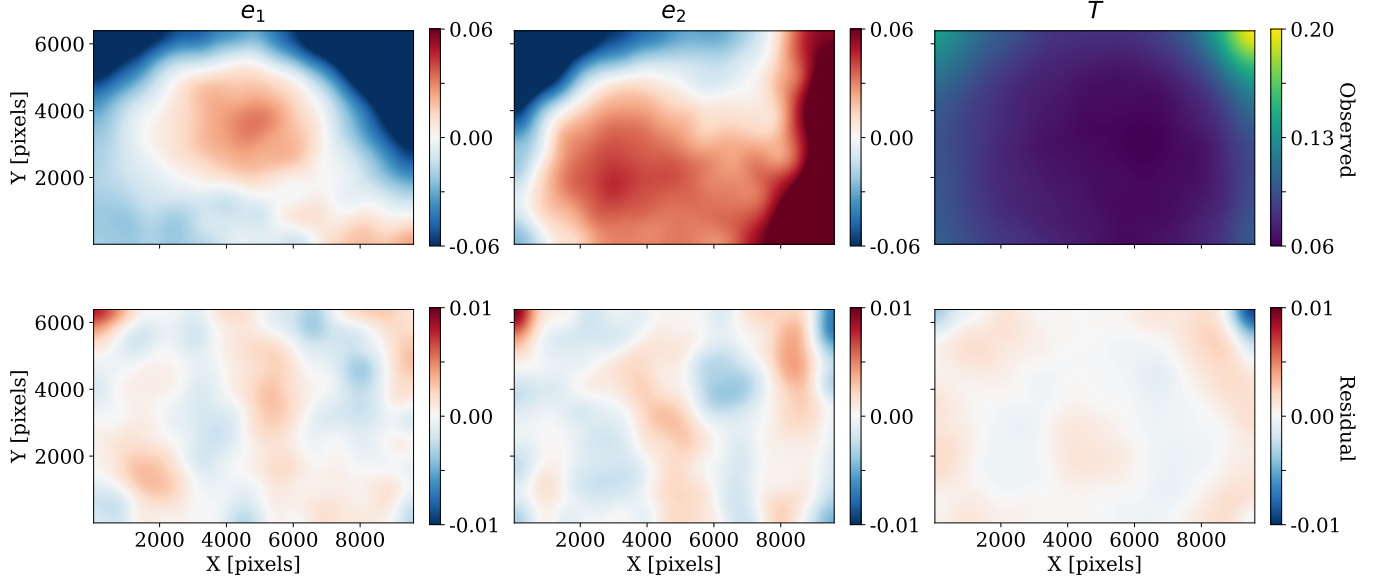


Figure 9. Spatial variability of stellar ellipticity and size across CCD coordinates. The top row shows ellipticity and size measurements of the reserved test stars, while the bottom row shows the residuals after subtracting the PSFEx model evaluated at the same positions.

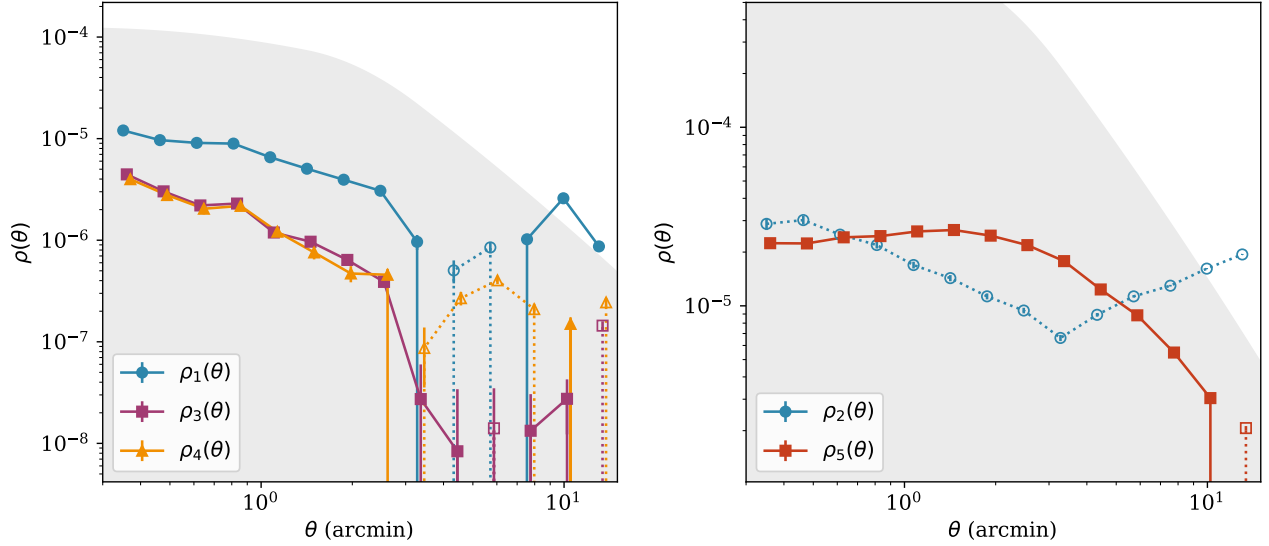


Figure 10. ρ statistics as defined in Eqs. 7–11. *Left:* ρ_1 (blue circles), ρ_3 (rose squares), and ρ_4 (orange triangles). *Right:* ρ_2 (blue circles) and ρ_5 (red squares). In both panels, dotted line segments indicate negative values. The statistics are computed using the 20% reserved test stars that were not included in PSF modeling; the sample includes stars from multiple exposures and targets. The shaded region indicates a “safe zone” corresponding to 5% of the expected shear two-point correlation function for a representative cluster with mean mass M_{500} and redshift z matching the SuperBIT sample. For this estimate, we adopt conservative values of $T_{\text{PSF}}/T_{\text{gal}} = 1$ and leakage strength $\alpha = 0.1$.

2016; J. Zuntz et al. 2018):

$$\delta\xi_+(\theta) = \left\langle \frac{T_{\text{PSF}}}{T_{\text{gal}}} \right\rangle^2 (\rho_1(\theta) + \rho_3(\theta) + \rho_4(\theta)) - \alpha \left\langle \frac{T_{\text{PSF}}}{T_{\text{gal}}} \right\rangle (\rho_2(\theta) + \rho_5(\theta)), \quad (6)$$

where the ρ 's are two-point statistics of PSF ellipticity and size residuals, defined as (B. Rowe 2010; M. Jarvis

et al. 2016):

$$\rho_1(\theta) \equiv \langle \delta e_{\text{PSF}}^*(\mathbf{x}) \delta e_{\text{PSF}}(\mathbf{x} + \theta) \rangle, \quad (7)$$

$$\rho_2(\theta) \equiv \langle e_{\text{PSF}}^*(\mathbf{x}) \delta e_{\text{PSF}}(\mathbf{x} + \theta) \rangle \quad (8)$$

$$\rho_3(\theta) \equiv \left\langle \left(e_{\text{PSF}}^* \frac{\delta T_{\text{PSF}}}{T_{\text{PSF}}} \right) (\mathbf{x}) \left(e_{\text{PSF}} \frac{\delta T_{\text{PSF}}}{T_{\text{PSF}}} \right) (\mathbf{x} + \theta) \right\rangle \quad (9)$$

$$\rho_4(\theta) \equiv \left\langle \delta e_{\text{PSF}}^*(\mathbf{x}) \left(e_{\text{PSF}} \frac{\delta T_{\text{PSF}}}{T_{\text{PSF}}} \right) (\mathbf{x} + \theta) \right\rangle \quad (10)$$

$$\rho_5(\theta) \equiv \left\langle e_{\text{PSF}}^*(\mathbf{x}) \left(e_{\text{PSF}} \frac{\delta T_{\text{PSF}}}{T_{\text{PSF}}} \right) (\mathbf{x} + \theta) \right\rangle, \quad (11)$$

We compute the ρ statistics using the reserved stars in each exposure, including stars from multiple exposures and targets, and present the results in Figure 10. For reference, we also show a shaded “safe zone” in the figure, defined as 5% of the expected galaxy two-point correlation signal from a cluster representative of the SuperBIT target sample with mean mass $M_{500} = 6.23 \times 10^{14} M_{\odot}$ and mean redshift $z = 0.245$. To estimate this safe zone, we adopt a deliberately conservative choice of $T_{\text{PSF}}/T_{\text{gal}} = 1$ and PSF leakage strength $\alpha = 0.1$. For the background galaxy redshift distribution, we use the COSMOS2015 catalog³³ (C. Laigle et al. 2016, 2021), convert the sources to SuperBIT F480W (b) band fluxes using their SEDs and the SuperBIT transmission curve shown in Figure 2 of (J. E. McCleary et al. 2023), and then simulate observations with a real SuperBIT PSF (the PSFEx solution derived from observations) and noise conditions. Our fiducial simulations are described in more detail in Section 5.4. We run our shape-measurement pipeline on these fiducial simulations and select objects using the selection criteria described in Section 4, yielding the expected redshift distribution of background sources for this analysis. The ρ -statistics analysis demonstrates that residual PSF modeling errors are sufficiently controlled to avoid significant contamination of the weak lensing signal within our requirements. All two-point statistics are computed using the TreeCorr package³⁴ (M. Jarvis et al. 2004).

4. SHAPE CATALOG

To reconstruct the weak-lensing signal, we require an observable that traces the shear field. The standard choice in weak-lensing analyses is the shape of galaxies, which is parameterized by a two-component ellipticity:

$$\mathbf{e} = e_1 + i e_2; \quad e_1 = e \cos(2\beta), \quad e_2 = e \sin(2\beta), \quad (12)$$

where e is the ellipticity amplitude and β is the position angle of the major axis measured counter-clockwise

³³ <https://irsa.ipac.caltech.edu/cgi-bin/Gator/nph-dd?catalog=cosmos2015>

³⁴ <https://github.com/rmjarvis/TreeCorr>

from the $+x$ image axis. Consistent with the moment-based definition in Eq. 2, the ellipticity of an object with elliptical isophotes can be expressed as

$$e = \frac{a - b}{a + b}, \quad (13)$$

with a and b the semi-major and semi-minor axes, respectively. In this convention, the ensemble average of galaxy ellipticities estimates the reduced shear,

$$\langle e \rangle \equiv g = \frac{\gamma}{1 - \kappa}, \quad (14)$$

with γ and κ denoting the shear and convergence, respectively.

The task of measuring galaxy shapes is highly non-trivial in the presence of observational effects such as the PSF, pixelization, and sky background noise. Since weak lensing is primarily concerned with the applied gravitational shear on galaxies, the problem can be reformulated: rather than requiring perfectly unbiased measurements of intrinsic ellipticity, one can instead quantify how the measured ellipticity of each galaxy responds to an applied external shear $\gamma = \gamma_1 + i\gamma_2$. If this shear response, R , can be estimated without bias, the weak-lensing shear field can be reconstructed even in the presence of non-ideal observational systematics. Several approaches to estimating this response exist (see R. Mandelbaum 2018 for a detailed review). In this work, we employ the METACALIBRATION algorithm (E. Huff & R. Mandelbaum 2017; E. S. Sheldon & E. M. Huff 2017).

4.1. METACALIBRATION Overview

The fundamental principle behind METACALIBRATION is to measure the shear response of a shape estimator \mathbf{e} directly from the data, rather than relying on simulations. The shape estimator can be expanded as a Taylor series in terms of a small applied shear γ :

$$\mathbf{e} = \mathbf{e}|_{\gamma=0} + \left. \frac{\partial \mathbf{e}}{\partial \gamma} \right|_{\gamma=0} \gamma + \dots, \quad (15)$$

where this relation holds at the per-object level. The per-object response is defined as

$$\mathbf{R}^{\gamma} = \left. \frac{\partial \mathbf{e}}{\partial \gamma} \right|_{\gamma=0}. \quad (16)$$

Numerically, the response can be estimated as

$$R_{ij}^{\gamma} = \frac{e_i^+ - e_i^-}{\Delta \gamma_j}, \quad (17)$$

where e_i^+ is the i -th ellipticity component measured on an image sheared by $+\gamma_j$, and e_i^- is the corresponding

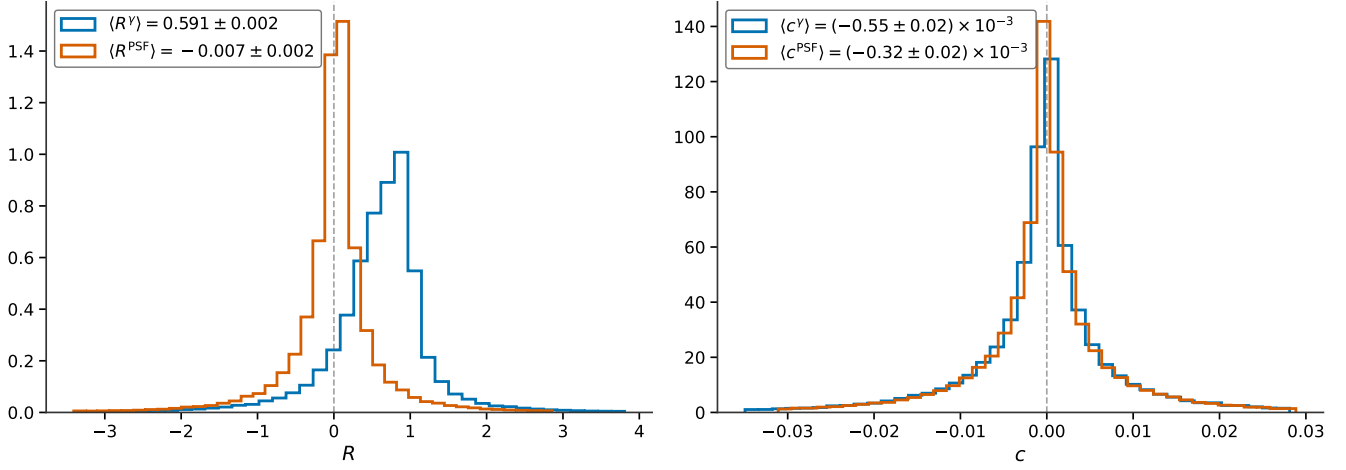


Figure 11. Distributions of per-object shear calibration quantities. *Left:* The galaxy shear response, R^γ (Eq. 17), and the PSF shear response, R^{PSF} (Eq. 18), with vertical dashed line marking $R = 0$. *Right:* The additive correction terms, c^γ and c^{PSF} (Eq. 19), with vertical dashed line marking $c = 0$. Legends report the mean values for each distribution.

measurement on an image sheared by $-\gamma_j$. The differential shear in the denominator is $\Delta\gamma_j = 2\gamma_j$; we adopt $\gamma_j = 0.01$.

We estimate these METACALIBRATION terms using the NGMIX package³⁵ (E. S. Sheldon 2014). For each object, NGMIX uses the discrete Fourier transform (DFT) of the PSF to deconvolve the galaxy image, applies an artificial shear in four directions (1+, 1-, 2+, 2-), and reconvolves the result with a slightly dilated version of the PSF using the `MetacalDilatePSF` class. Since this process does not yield a perfectly round PSF kernel, it is necessary to account for additive shear bias using PSF shear terms produced by NGMIX.

Thus, to calculate the shear response, we construct a dictionary of five image versions for each galaxy: {`noshear`, 1+, 1-, 2+, 2-}. (Here, `noshear` refers to deconvolution and reconvolution of the galaxy image with no artificial shear applied.) In addition, we produce four PSF shear terms: {`PSF1+`, `PSF1-`, `PSF2+`, `PSF2-`}, where only the reconvolution PSF is sheared (the galaxy image remains unsheared). With these terms, we can similarly estimate the per-object PSF response:

$$R_{ij}^{\text{PSF}} = \frac{e_i^{\text{PSF},+} - e_i^{\text{PSF},-}}{\Delta\gamma_j}, \quad (18)$$

where $e_i^{\text{PSF},+}$ is the i -th ellipticity measured on an image convolved with a PSF sheared by $+\gamma_j$, and $e_i^{\text{PSF},-}$ is the corresponding measurement for $-\gamma_j$. In this case, as well, we adopt $\Delta\gamma_j = 2\gamma_j = 0.02$.

Finally, to correct for any surviving additive bias, we calculate additive terms for both galaxy shear and PSF

shear as (E. Huff & R. Mandelbaum 2017)

$$\begin{aligned} \mathbf{c}^\gamma &= \frac{\mathbf{e}^+ + \mathbf{e}^-}{2} - \mathbf{e}_{\text{noshear}}, \\ \mathbf{c}^{\text{PSF}} &= \frac{\mathbf{e}^{\text{PSF},+} + \mathbf{e}^{\text{PSF},-}}{2} - \mathbf{e}_{\text{noshear}}. \end{aligned} \quad (19)$$

If we finally take the ensemble average of Eq. 15, we can write

$$\langle \mathbf{e} \rangle = \langle \mathbf{e} \rangle |_{\gamma=0} + \langle \mathbf{R}^\gamma \gamma \rangle. \quad (20)$$

In the presence of additive bias, the mean ellipticity at zero shear can be expressed as

$$\langle \mathbf{e} \rangle |_{\gamma=0} = \langle \mathbf{c}^\gamma \rangle + \langle \mathbf{c}^{\text{PSF}} \rangle \equiv \langle \mathbf{c}^{\text{total}} \rangle. \quad (21)$$

The additive biases are typically of order 10^{-4} . Figure 11 shows the distributions of the multiplicative response and the additive correction for the final galaxy sample. With these ingredients, the final form of the weighted-average shear estimator is given by

$$\langle \gamma \rangle \approx \langle \mathbf{R}^\gamma \rangle^{-1} \left(\langle \mathbf{e} \rangle - \langle \mathbf{c}^{\text{total}} \rangle \right). \quad (22)$$

We account for shear-dependent selection effects described in (E. S. Sheldon & E. M. Huff 2017) with a selection response for an artificially applied shear, defined as

$$\langle R^S \rangle_{ij} = \frac{\langle e_i \rangle^{S+} - \langle e_i \rangle^{S-}}{\Delta\gamma_j}, \quad (23)$$

where $\langle e_i \rangle^{S+}$ corresponds to the mean of the i th ellipticity component measured on the *unsheared* images, but for the sample selected using the images sheared by $+\gamma_j$, and similarly for $\langle e_i \rangle^{S-}$. The total response is then obtained as

$$\langle \mathbf{R} \rangle = \langle \mathbf{R}^\gamma \rangle + \langle \mathbf{R}^S \rangle. \quad (24)$$

³⁵ <https://github.com/esheldon/ngmix>

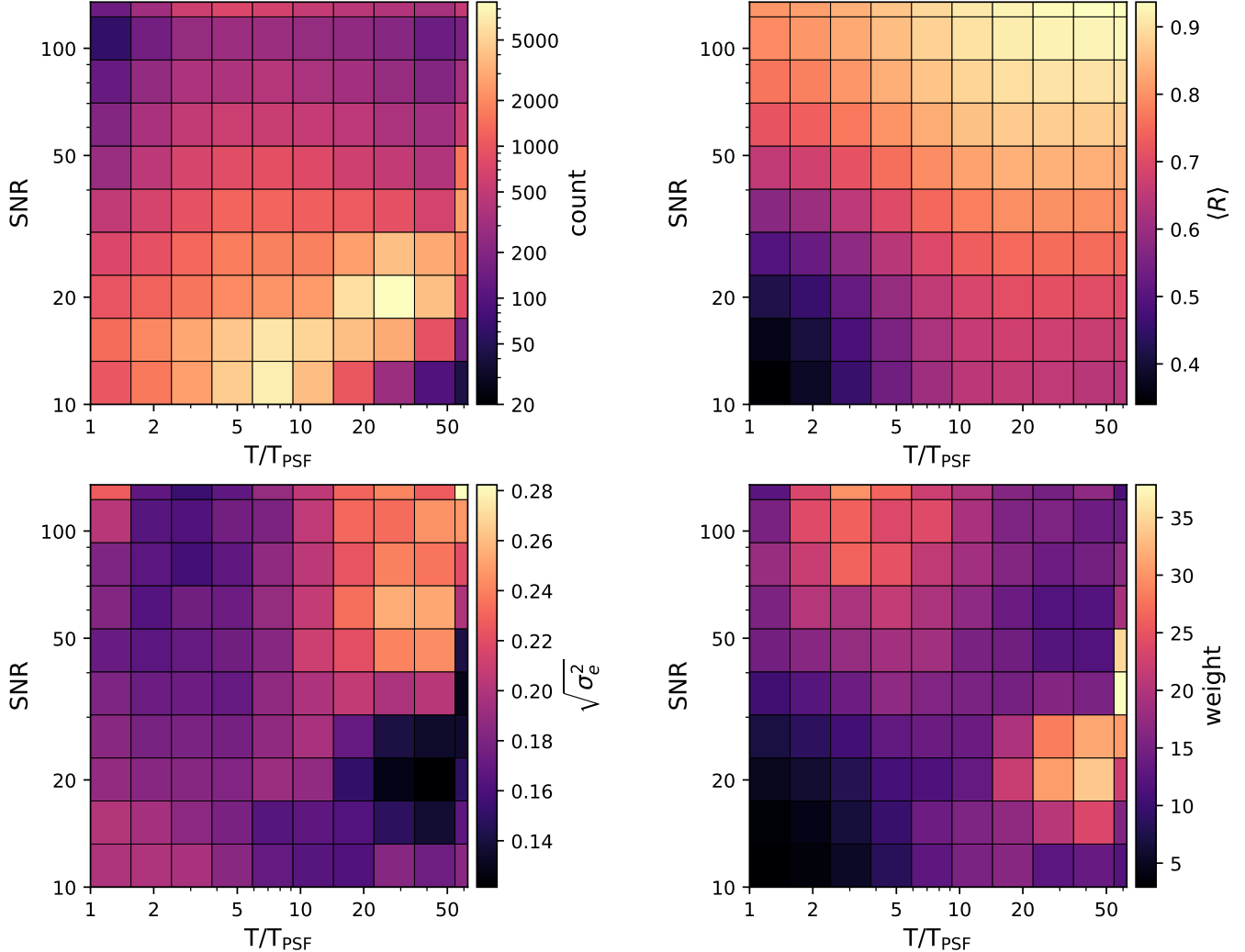


Figure 12. Several statistics of the catalog as a function of METACALIBRATION quantities: counts (upper left), $\sqrt{\langle\sigma_{1,2}^2\rangle}$ (lower left), response R_γ (upper right), and weight as defined in Eq. 27 (lower right), shown as a function of gridded SNR and T/T_{PSF} parameter space. The grids have been chosen to include 95% of the objects in a 10×10 logarithmic bin and all objects above 95 percentile have been accumulated in the last bin.

4.2. Object selection for METACALIBRATION

Object selection is one of the most critical steps in weak-lensing analyses, as it directly impacts the fidelity of the final cosmological constraints and mass reconstructions. The aim is to maximize statistical power while ensuring that the METACALIBRATION response remains stable as a function of measurement-noise proxies. We select galaxies based on (i) the SNR of the galaxy model fit and (ii) the ratio of the intrinsic galaxy size to the PSF size at the galaxy’s position.

NGMIX provides an estimate of the SNR as part of the model-fitting process for each galaxy. This SNR corresponds to a matched-filtering estimate of the fitted

model and is defined as

$$\text{SNR} = \frac{\sum_p \frac{m_p I_p}{\sigma_p^2}}{\left(\sum_p \frac{m_p^2}{\sigma_p^2}\right)^{1/2}}, \quad (25)$$

where the sum runs over image pixels p , m_p is the profile of the best-fit galaxy model in pixel space, I_p is the observed pixel intensity, and σ_p is the pixel noise standard deviation.

The second proxy, T/T_{PSF} , quantifies the relative size of the galaxy with respect to the PSF, where T denotes the pre-PSF galaxy size. By “pre-PSF” we mean the size parameter of the best-fit galaxy model before convolution with the best-fit PSF model, as inferred from the full Bayesian forward-modeling framework implemented

in NGMIX. A brief overview of the NGMIX workflow is provided in Appendix B.

Based on these measurement quantities, we apply a set of selection cuts to define our METACALIBRATION catalog. Our choices closely follow the criteria used in the SuperBIT forecasting analysis (J. E. McCleary et al. 2023) and the DES Y3 weak lensing analysis (M. Gatti et al. 2021). Specifically, we impose:

1. $10 < \text{SNR} < 1000$,
2. $\frac{T}{T_{\text{PSF}}} > 0.5$,
3. $T < 10$,

We adopt a gridding approach to calculate the shear response R_γ defined over the SNR- T/T_{PSF} parameter space. Each galaxy is assigned an R_γ value corresponding to its grid cell. As demonstrated in Section 5.4, this gridded estimation of the response substantially reduces shear bias. In addition to the shear response, we include a global selection response term estimated from the full sample rather than from the SNR- T/T_{PSF} grid. The final, response-calibrated shapes in our catalog are obtained by dividing by the total response. In addition to these cuts, we apply color-based selections and red-sequence matching to separate foreground galaxies from background sources when reconstructing the weak-lensing signal (i.e., convergence maps). The details of this selection will be presented in the *Lensing in the Blue IV: Convergence Maps* paper (Saha et al. 2026, in prep.).

4.3. Weights

To obtain a high-fidelity shear signal from the source catalog, it is important to assign weights to galaxies based on the precision of their shape measurements. Intuitively, objects with more precise measurements should contribute more strongly, while noisier measurements should be down-weighted.

We follow the weighting scheme adopted in M. Yamamoto et al. (2025); M. Gatti et al. (2021); D. Anbagane et al. (2025), in which weights are derived in a two-dimensional parameter space of SNR and size ratio T/T_{PSF} . Specifically, we bin the galaxies in this space, and within each bin estimate the shape noise variance σ_e^2 and the mean shear response $\langle R^\gamma \rangle$, where $\langle R^\gamma \rangle$ is the average of the diagonal components R_{11}^γ and R_{22}^γ . The weight assigned to galaxies in bin (i, j) is then defined as

$$w_{ij} = \frac{\langle R^\gamma \rangle_{ij}^2}{(\sigma_e^2)_{ij}}, \quad (26)$$

where i and j index the size ratio and SNR bins, respectively. The shape noise variance in each bin is estimated

as

$$(\sigma_e^2)_{ij} = \frac{1}{N_{ij}} \sum_{k=1}^{N_{ij}} (e_{k,1}^2 + e_{k,2}^2), \quad (27)$$

where N_{ij} is the number of galaxies in bin (i, j) , and the sum runs over all galaxies in that bin. Figure 12 shows the binned distributions of the raw galaxy counts, $\sqrt{\sigma_e}$, $\langle R^\gamma \rangle$, and the weight w in a 10×10 logarithmic grid. The upper bounds of the parameter space are chosen to include 95% of the sample, with galaxies at higher SNR or T/T_{PSF} accumulated in the final bins. Galaxies are then assigned weights based on their corresponding bin, or the nearest bin if they lie outside the defined range.

4.4. Number Density

For any weak-lensing shape catalog, it is essential to quantify the statistical power available for constraining physical parameters. This is typically characterized by the weighted effective source number density. Following the definition in C. Heymans et al. (2012), we compute

$$n_{\text{eff}} = \frac{1}{A} \frac{(\sum_i w_i)^2}{\sum_i w_i^2}, \quad (28)$$

where A is the survey area, and w_i is the weight of galaxy i , obtained from the gridded SNR- T/T_{PSF} space. Effective source densities for all targets are presented in Table 2.

4.5. Empirical Tests of the Shape Catalog

An essential requirement for galaxy shape measurements within the NGMIX framework is that the best-fit Gaussian mixture model accurately represents the PSF interpolated by PSFEX at the position of each galaxy. We investigate this requirement in detail in Appendix B. In this section, we instead examine the shape catalog for potential residual systematics arising from imperfect PSF modeling. Specifically, we test whether the measured galaxy shapes show correlations with PSF properties. We also examine correlations with galaxy properties used to define selection cuts in the METACALIBRATION process. Any significant dependence of the measured shapes on quantities such as the SNR or T/T_{PSF} would indicate residual systematics in the shape-measurement pipeline.

To assess this, we compute the Pearson correlation matrix between the measured galaxy shear components, PSF ellipticities, and relevant galaxy properties. The Pearson correlation coefficient, r_{xy} , between two quantities x and y is defined as

$$r_{xy} = \frac{\text{Cov}(x, y)}{\sigma_x \sigma_y}, \quad (29)$$

Table 2. Summary of source number densities for the SuperBIT targets. The target type, sky position, redshift and three estimates of the source number density are shown for each target. The “Raw” column gives the source density after removing stars and applying masks. The “Selected” column reports the unweighted source density after applying the selection cuts described in Section 4.1. The final column, n_{eff} , shows the effective weighted source number density of selected objects as defined in Eq. 28.

Target	Target Type	RA (deg)	Dec (deg)	Redshift	Raw (arcmin ⁻²)	Selected (arcmin ⁻²)	n_{eff} (H12) (arcmin ⁻²)
1E0657 Bullet	Merging Clusters	104.61450	-55.95475	0.296	22.87	18.91	14.52
Abell 141	Merging Clusters	16.40085	-24.66079	0.230	11.36	10.00	8.31
Abell 1689	Merging Clusters	197.87025	-1.34168	0.183	22.17	20.81	17.22
Abell 2163	Merging Clusters	243.94512	-6.14784	0.203	15.00	11.62	8.93
Abell 2345	Merging Clusters	321.78648	-12.16679	0.179	18.45	16.12	12.90
Abell 2384a	Merging Clusters	328.09425	-19.56626	0.094	20.35	18.00	14.28
Abell 2384b	Merging Clusters	328.03567	-19.72170	0.094	16.45	14.08	10.73
Abell 3192	Merging Clusters	59.71568	-29.94346	0.425	15.96	13.95	10.85
Abell 3365	Merging Clusters	87.19233	-21.92990	0.093	11.40	8.19	6.15
Abell 3411	Merging Clusters	130.45046	-17.49227	0.162	21.40	17.09	13.05
Abell 3526	Merging Clusters	192.19688	-41.30712	0.011	20.60	13.31	7.81
Abell 3571	Merging Clusters	206.87965	-32.86029	0.039	20.27	15.58	11.34
Abell 3667	Merging Clusters	303.15580	-56.84331	0.056	18.45	13.80	10.54
Abell 3716S	Merging Clusters	312.98849	-52.69637	0.045	17.74	14.98	11.52
Abell 3827	Merging Clusters	330.43705	-59.95795	0.098	16.30	14.23	11.17
Abell S0592	Merging Clusters	99.68232	-53.97385	0.222	22.55	19.37	15.65
ACT-CL J0012.8-0855	Filament	3.21349	-8.91999	0.338	12.10	10.77	8.81
ACT-CL J0411.2-4819	Merging Clusters	62.81384	-48.32236	0.418	20.09	--	--
MACS J0416.1-2403	Merging Clusters	64.03787	-24.07053	0.397	11.40	10.33	8.40
MACS J1105.7-1014	Merging Clusters	166.45958	-10.25243	0.466	13.81	12.37	9.57
MACS J1931.8-2635	Merging Clusters	292.95667	-26.57583	0.352	28.49	8.23	4.86
MS1008.1-1224	Merging Clusters	152.60835	-12.65294	0.306	15.89	14.15	11.04
MS2137-2353	Merging Clusters	325.06132	-23.66031	0.313	14.08	11.28	8.43
PLCK G287.0+32.9	Merging Clusters	177.70640	-28.08444	0.383	17.80	15.50	12.03
RXC J1314.4-2515	Merging Clusters	198.63567	-25.26848	0.244	15.20	12.64	9.77
RXC J1514.9-1523	Merging Clusters	228.76418	-15.36761	0.223	18.16	14.39	11.02
RXC J2003.5-2323	Merging Clusters	300.88723	-23.40022	0.317	17.30	10.49	7.15
RX J1347.5-1145	Merging Clusters	206.872788	-11.745483	0.451	17.18	14.94	11.78
SMACSJ0723.3-7327	Merging Clusters	110.85730	-73.43672	0.390	18.83	13.36	9.89
SMACSJ2031.8-4036	Exotic Lens	307.96747	-40.61824	0.331	23.56	19.41	14.95
Z20-SPT-CLJ0135-5904	Merging Clusters	23.97592	-59.10169	0.490	20.55	19.71	16.87
COSMOS113	Calibration field	149.85274	1.75418	--	12.25	10.85	8.49
COSMOSa	Legacy tile	150.29180	1.90032	--	14.77	13.06	10.66
COSMOSb	Legacy tile	150.05422	1.86288	--	15.68	14.21	11.49
COSMOSg	Legacy tile	150.08010	2.56667	--	18.03	16.91	13.99
COSMOSk	Legacy tile	150.22175	2.23472	--	15.38	13.95	11.29
COSMOSo	Legacy tile	150.26667	2.45508	--	13.64	11.86	9.20

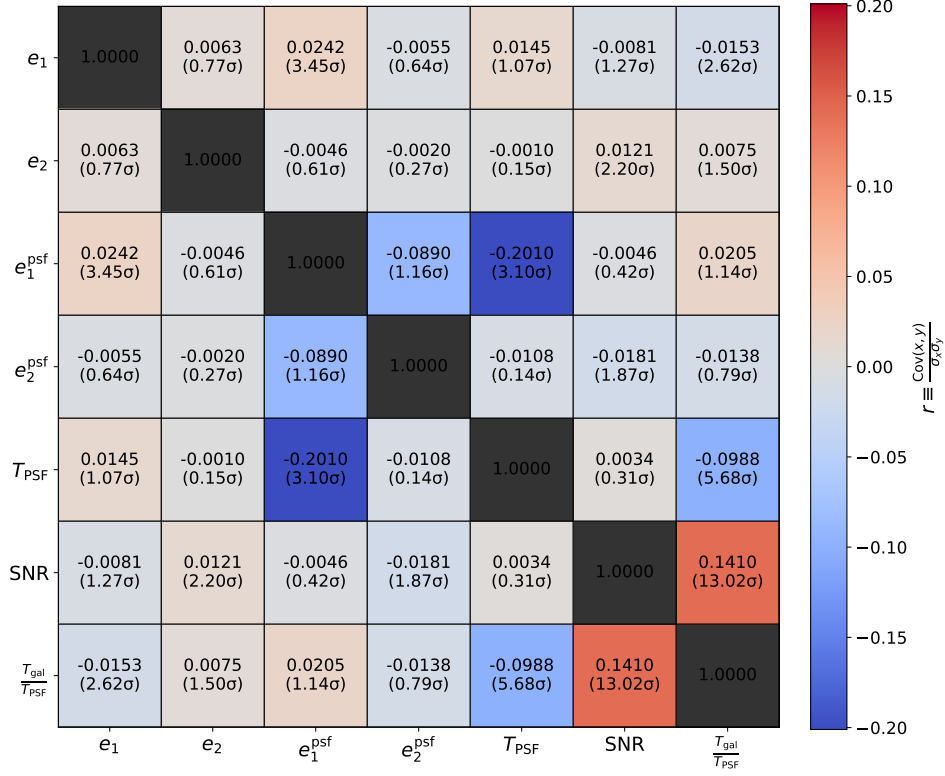


Figure 13. The Pearson correlation matrix quantifying the correlations between galaxy shear components and PSF properties, including the PSF ellipticity components (e_i^{PSF}) and PSF size (T_{PSF}), as well as key METACALIBRATION quantities such as the SNR and the galaxy-PSF size ratio.

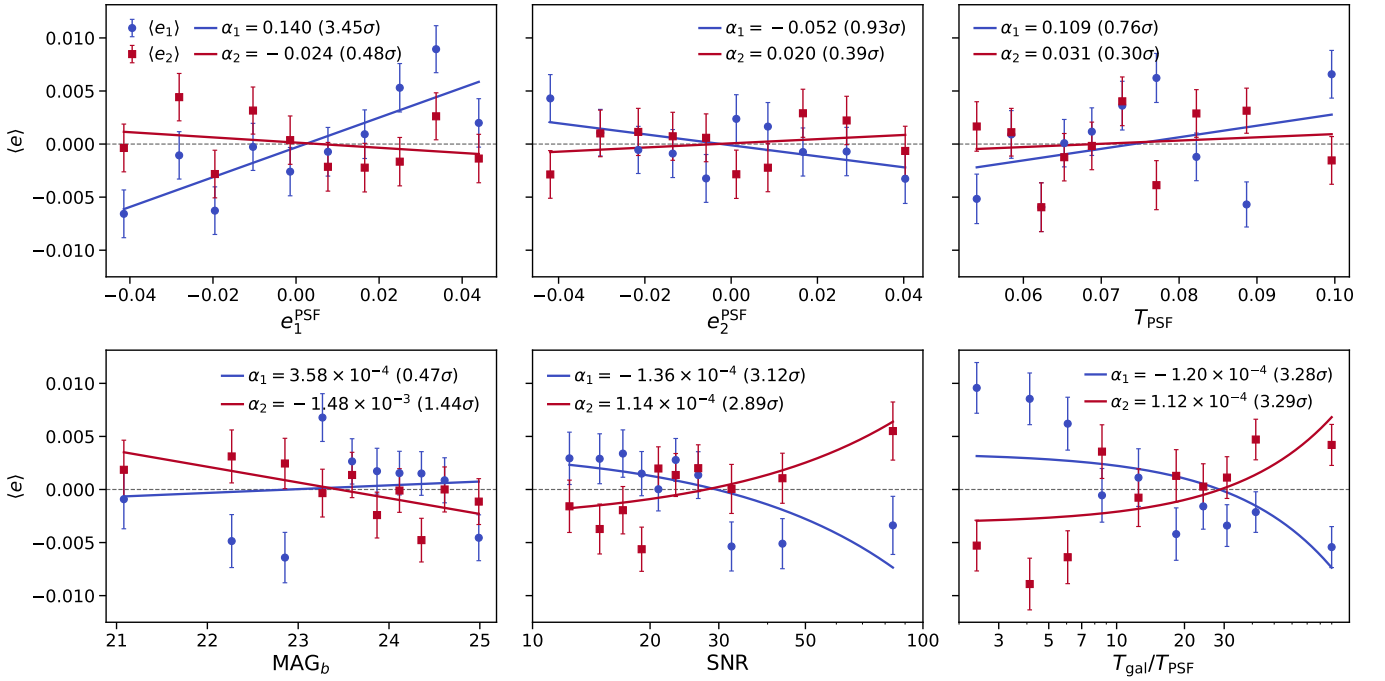


Figure 14. Mean Shear dependence as a function of PSF and Galaxy quantities, in percentile bins. The Blue circles and red squares denotes the mean shear $\langle e_1 \rangle$, $\langle e_2 \rangle$ values respectively in each bin. The corresponding solid lines depicts the best fit linear model, showing the slope α 's in the legend

where $\text{Cov}(x, y)$ denotes the covariance between the two quantities, and σ_x and σ_y are their respective standard deviations used to normalize the covariance and obtain the correlation coefficient. Prior to computing the correlations, we subtract the global mean shear from the catalog to remove any residual offsets.

The resulting Pearson correlation matrix is presented in Figure 13. Statistical uncertainties on each correlation coefficient are estimated using a jackknife resampling of the full catalog into 30 subsets. Each matrix element reports the correlation coefficient along with its significance, quantified as r/σ_r .

Upon closer inspection of the Pearson correlation matrix, we find a strong correlation between the SNR (Eq. 25) of the galaxy parameter fit and T/T_{PSF} . This behavior is expected, as the size ratio quantifies how well resolved a galaxy is relative to the PSF: better-resolved galaxies yield more reliable shape measurements and consequently higher SNR values, and vice versa. We also observe a significant anti-correlation between the PSF ellipticity component e_1^{PSF} and the PSF size T_{PSF} . This reflects an intrinsic property of the PSF and is consistent with the spatial PSF residual patterns shown in the upper panel of Figure 9. In particular, regions where e_1^{PSF} is more positive correspond to smaller PSF sizes near the center of the CCD, whereas regions with more negative e_1^{PSF} exhibit larger PSF sizes toward the corners.

Finally, we detect a non-zero correlation between the galaxy shear component e_1 and the corresponding PSF ellipticity e_1^{PSF} , which warrants further investigation. To quantify potential leakage of PSF or galaxy-property correlations into the measured shear, we examine the dependence of the mean galaxy shear on several quantities of interest using a linear model parameterized by a leakage coefficient α . We bin galaxies into percentile bins of quantities including e_1^{PSF} , e_2^{PSF} , T_{PSF} , MAG_b , SNR, and the size ratio $T_{\text{gal}}/T_{\text{PSF}}$. Within each bin, we compute the weighted mean galaxy shear components $\langle e_1 \rangle$ and $\langle e_2 \rangle$. We then fit a linear model to the binned measurements,

$$\langle e_{1,2} \rangle = \alpha_{1,2} X + \beta_{1,2}, \quad (30)$$

where X denotes the quantity under consideration. A statistically significant non-zero value of α indicates a correlation between the mean shear and the corresponding quantity.

The results of these diagnostics are presented in Figure 14. Blue and red points show the binned mean shear measurements, while the solid lines of matching colors indicate the best-fitting linear relations. The fitted α values are reported in the legends of each panel. Uncer-

tainties on α are estimated using jackknife resampling of the full catalog, following the same procedure used for the Pearson correlation coefficient uncertainties. Consistent with the Pearson matrix, we find a statistically significant correlation between the mean galaxy shear $\langle e_1 \rangle$ and the PSF ellipticity e_1^{PSF} , with $\alpha_1 = 0.140$, corresponding to a 3.45σ detection. We investigate this correlation further using our fiducial simulations in Section 5.4.3.

5. PIPELINE VALIDATION

5.1. Image simulation framework

Our simulation framework for validating the SuperBIT shape-measurement pipeline closely follows the methodology described in J. E. McCleary et al. (2023). In brief, we generate synthetic CCD images by injecting realizations of galaxies and stars into blank exposures. Galaxy injection parameters are drawn from the COSMOS2015 catalog, with object fluxes converted to SuperBIT bands using their spectral energy distributions (SEDs) and the SuperBIT transmission curves. The background galaxy population is lensed using an NFW cluster model with mass $M_{200} = 4.1 \times 10^{14} M_{\odot}$ at redshift $z = 0.24$. For each injected galaxy, the applied shear and magnification are computed using its corresponding source redshift, drawn from the COSMOS catalog. Instrumental and observational effects are included by adding dark current, detector noise, and an approximate sky background appropriate for stratospheric observing conditions (A. Gill et al. 2020). We also apply small dithers between exposures to mimic the pointing variations present in real observations. The final images are then processed through the full lensing analysis pipeline described above.

5.2. Shear recovery metric

To quantify the end-to-end performance of the pipeline, we test how accurately it recovers the tangential shear profile of the input NFW lens. For each galaxy at position (x, y) relative to a chosen reference centre (x_c, y_c) , the tangential and cross shear components are defined as

$$\gamma_+ = -[\gamma_1 \cos(2\phi) + \gamma_2 \sin(2\phi)], \quad (31)$$

$$\gamma_{\times} = \gamma_1 \sin(2\phi) - \gamma_2 \cos(2\phi), \quad (32)$$

where ϕ is the azimuthal angle with respect to the reference centre,

$$\phi = \tan^{-1} \left(\frac{y - y_c}{x - x_c} \right). \quad (33)$$

We bin galaxies into annuli and compute the weighted mean tangential shear in each radial bin, denoted $\hat{\gamma}_{+,k}$,

Table 3. Estimated $\hat{\zeta}$ and its 1σ uncertainty for the sequence of unit-test simulations described in Section 5.3.

Seq.	Simulation setup	$\hat{\zeta}$	$\sigma_{\hat{\zeta}}$
1	Constant galaxy properties + Gaussian PSF	0.9885	0.0612
2	Constant galaxy properties + SuperBIT PSF	1.0143	0.0682
3	COSMOS size distribution + SuperBIT PSF	1.0078	0.0564
4	COSMOS size + magnitude distributions + SuperBIT PSF	0.9775	0.0987

where k indexes the radial bins. Because the input lens model is known, we compare the recovered binned profile $\hat{\gamma}_+$ to the truth prediction γ_+^{true} and parametrize the overall multiplicative recovery factor as

$$\zeta \equiv \frac{\langle \hat{\gamma}_+ \rangle}{\gamma_+^{\text{true}}}. \quad (34)$$

An unbiased recovery corresponds to $\zeta = 1$, while deviations from unity indicate residual systematic shear bias.

Following J. E. McCleary et al. (2023), we estimate ζ using a maximum-likelihood estimator

$$\hat{\zeta} = \frac{\gamma_+^{\text{true T}} \mathbf{C}^{-1} \hat{\gamma}_+}{\gamma_+^{\text{true T}} \mathbf{C}^{-1} \gamma_+^{\text{true}}}, \quad (35)$$

with variance

$$\sigma_{\hat{\zeta}}^2 = (\gamma_+^{\text{true T}} \mathbf{C}^{-1} \gamma_+^{\text{true}})^{-1}. \quad (36)$$

Here \mathbf{C} is the covariance matrix of the binned recovered tangential shear profile $\hat{\gamma}_+$. In this work we approximate \mathbf{C} as diagonal, with diagonal elements given by the variance of $\hat{\gamma}_{+,k}$ in each annulus.

To characterize the statistical uncertainty, we generate an ensemble of $N_{\text{sim}} = 30$ independent realizations of the same lensed field, varying (i) the COSMOS galaxies drawn for injection, (ii) their random orientations, and (iii) the detector-noise realization. For each simulation realization j , galaxies are binned radially and the weighted mean tangential shear $\hat{\gamma}_{+,k}^{(j)}$ is computed in each annular bin k .

The covariance matrix \mathbf{C} is constructed to include both the scatter of galaxy shears within each annulus and the realization-to-realization variance across simulations. In practice, the diagonal element for bin k is estimated as the variance of the mean tangential shear across realizations,

$$C_{kk} = \frac{1}{N_{\text{sim}} - 1} \sum_{j=1}^{N_{\text{sim}}} \left(\hat{\gamma}_{+,k}^{(j)} - \langle \hat{\gamma}_{+,k} \rangle \right)^2, \quad (37)$$

where

$$\langle \hat{\gamma}_{+,k} \rangle = \frac{1}{N_{\text{sim}}} \sum_{j=1}^{N_{\text{sim}}} \hat{\gamma}_{+,k}^{(j)} \quad (38)$$

denotes the mean over realizations. Since each $\hat{\gamma}_{+,k}^{(j)}$ is itself a weighted mean over galaxies in that radial bin k , this variance naturally captures both the intrinsic shape noise within each realization and the scatter between different realizations.

5.3. Incremental Unit Tests

We perform a sequence of controlled ‘‘unit-test’’ simulations, broadly following the philosophy of the DES Y3 simulation validation (N. MacCrann et al. 2021). Starting from highly idealized images, we incrementally increase the realism to isolate the dominant contributors to shear bias.

For these unit tests, galaxies are injected on a square grid lattice to eliminate blending, which is often a leading source of shear bias. Stars are placed on an interleaved grid to avoid overlap with galaxies and to ensure well-conditioned PSF estimation. We consider the following sequence:

1. **Constant galaxy properties + Gaussian PSF:** all galaxies have fixed magnitude $m = 20$ and fixed half-light radius $r_{1/2} = 0.5''$, with a Gaussian PSF of FWHM $0.5''$.
2. **Constant galaxy properties + SuperBIT PSF:** identical to (1), but replacing the Gaussian PSF with an empirical SuperBIT PSF model derived from real data using PSFEX.
3. **COSMOS size distribution:** identical to (2), but sampling galaxy sizes from COSMOS (restricted to $r_{1/2} \leq 1''$).
4. **COSMOS magnitude distribution:** identical to (3), but additionally sampling magnitudes from COSMOS, with fluxes converted to SuperBIT bands as described in Section 5.1.

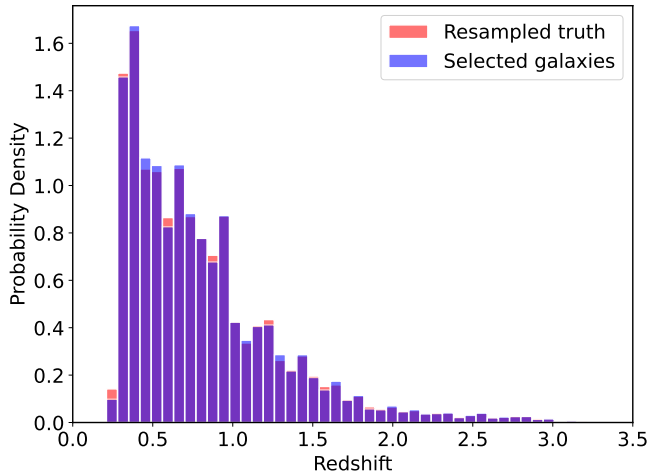


Figure 15. Redshift distribution of background galaxies in the fiducial simulations for a cluster at redshift $z = 0.245$. The blue histogram shows the redshift distribution of detected galaxies that pass the METACALIBRATION selection criteria, while the red histogram shows the resampled redshift distribution of the injected galaxies used to estimate the true tangential shear, γ_+^{true} .

We report the recovered $\hat{\zeta}$ for each configuration in Table 3.

5.4. Fiducial simulation

As the final step in our progression toward increasing realism, we move from gridded galaxy injections to a random spatial injection of galaxies. This transition naturally introduces source blending. All other aspects of the simulation pipeline remain identical to those used in the final unit tests; in particular, galaxy properties are sampled from the COSMOS catalog.

For the first three unit-test configurations, all injected galaxies are detected in the coadded image. This is a direct consequence of the simplified simulation setup, in which galaxies are assigned constant, relatively bright magnitudes, resulting in a detection efficiency close to unity. In contrast, for unit test 4, galaxy magnitudes are sampled from the COSMOS catalog. As expected, this leads to a significantly reduced detection fraction of $\sim 20\%$. A comparable detection fraction is obtained in the fiducial simulations, which adopt the same realistic galaxy population but with random spatial injections.

In these latter two cases, the true tangential shear profile γ_+^{true} must be evaluated using a source redshift distribution that matches the population of galaxies selected for shape measurement. Accordingly, we resample the injected galaxy redshift distribution to match the redshift distribution of the detected galaxies that pass the METACALIBRATION selection criteria. The red-

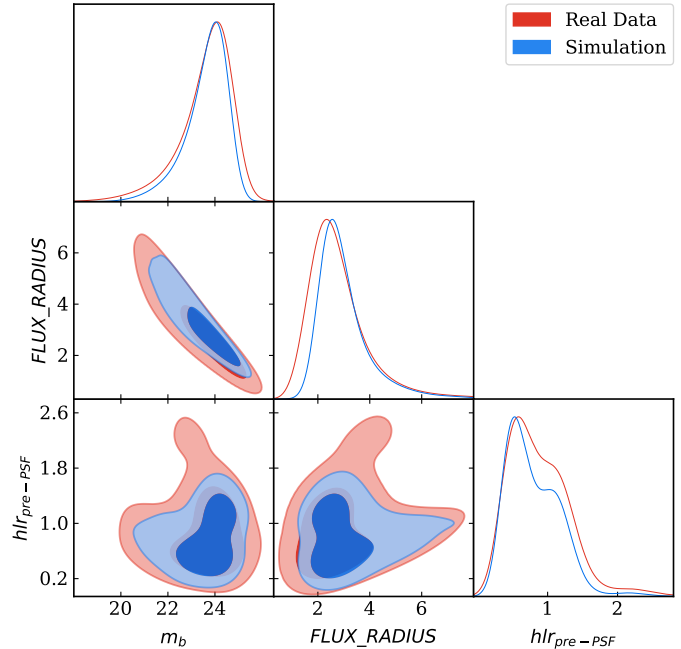


Figure 16. Comparison of one-dimensional and joint two-dimensional distributions of galaxy properties in the b band: magnitude (m_b), FLUX_RADIUS (post-PSF half-light radius), and pre-PSF half-light radius (hlr). Red contours correspond to real data, while blue contours correspond to the fiducial simulations.

shift distribution of the selected galaxies for our fiducial simulations, together with the corresponding resampled injected redshift distribution, is shown in Figure 15.

5.4.1. Representativeness of Fiducial Simulations

To validate the shear reconstruction achieved by our pipeline, it is essential to establish that the fiducial simulations are statistically representative of the real data. We perform this validation by comparing one-dimensional and joint two-dimensional distributions of several key galaxy properties measured in the main science band F480W (b). These include the galaxy magnitude m_b , the SExtractor quantity FLUX_RADIUS (the post-PSF half-light radius in units of image pixels), and the pre-PSF half-light radius (hlr), which is derived from the best-fit galaxy size parameter output by NGMIX as T_noshear. The size parameter T is defined as the trace of the second-order moment matrix of the pre-PSF galaxy light profile (Eq. 1). For a Gaussian surface-brightness profile, the corresponding half-light radius is

$$\text{hlr} = \sqrt{\frac{T}{2}} \sqrt{2 \ln 2}, \quad (39)$$

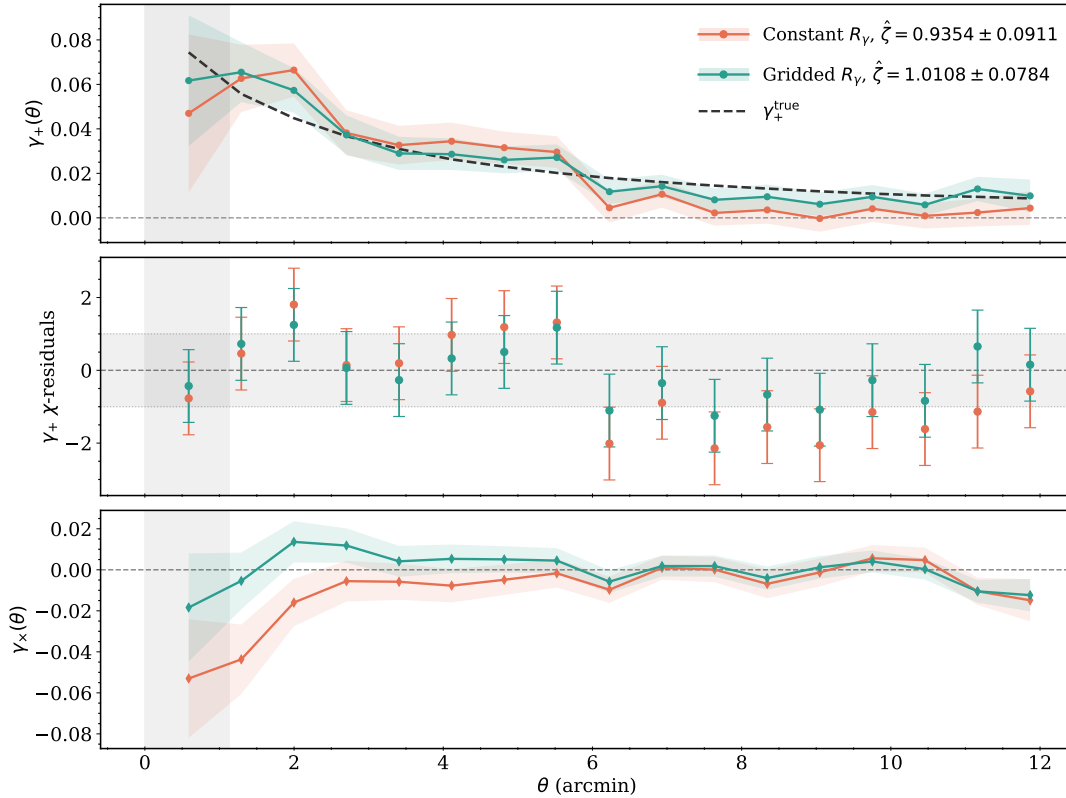


Figure 17. Tangential shear bias estimation in the fiducial simulations. The coral color corresponds to the constant shear calibration approach, while the teal color corresponds to the gridded shear calibration approach. The vertical grey shaded region indicates the excluded range of the shear-bias estimation, where the applied shear is sufficiently large that the linearized implementation of METACALIBRATION is no longer valid. *Upper panel:* Reconstructed tangential shear γ_+ for both calibration approaches. The injected NFW shear profile, γ_+^{true} , is shown as a black dashed curve. The corresponding estimates of $\hat{\zeta}$ for both approaches, computed using Eq. 35, are indicated in the legend. *Middle panel:* χ -residuals for all data points for both calibration approaches. The horizontal shaded band denotes a reference region around zero, $-1 \leq \chi \leq +1$. *Lower panel:* Reconstructed cross-shear profiles for both approaches.

and is expressed in units of arcseconds. The joint and marginal distributions of these quantities are shown in the triangular (corner) plot presented in Figure 16³⁶

5.4.2. Shear-bias estimation

To validate the shear reconstruction in our fiducial simulations, we apply the tangential shear bias formalism described in Section 5.2, and present the results in Figure 17. We compare two distinct shear-calibration strategies.

The first approach employs the conventional calibration scheme based on a global mean shear response derived from the selected galaxy sample, combined with a global selection response to calibrate individual galaxy shapes. This conventional calibration method is shown in coral in Figure 17 and yields $\hat{\zeta} = 0.935 \pm 0.091$. Since

the only structural difference between Unit Test 4 and the fiducial simulation is the transition from gridded galaxy injections to randomly distributed galaxies, we attribute this bias primarily to source blending.

Motivated by this result, we apply the same gridded shear-response calibration scheme used for the real data (Section 4.2) to the fiducial simulations. Each galaxy is assigned a shear response based on its location in the $(\text{SNR}, T/T_{\text{PSF}})$ grid, and a global selection response is combined with the gridded shear response to obtain the final calibration. The diagonal elements of the global selection response estimated from the fiducial simulations are $R_{11}^S = -0.022 \pm 0.052$ and $R_{22}^S = 0.058 \pm 0.055$.

This approach leads to a substantial improvement in shear recovery, yielding $\hat{\zeta} = 1.011 \pm 0.078$, consistent with unbiased shear reconstruction. For both calibration methods, we exclude the regime $\gamma_+^{\text{true}} \geq 0.06$, where the applied shear is sufficiently large that the linearized implementation of METACALIBRATION is no longer valid (E. S. Sheldon & E. M. Huff 2017). This excluded re-

³⁶ The figure was generated using GETDIST (<https://github.com/cmbant/getdist>) (A. Lewis 2025).

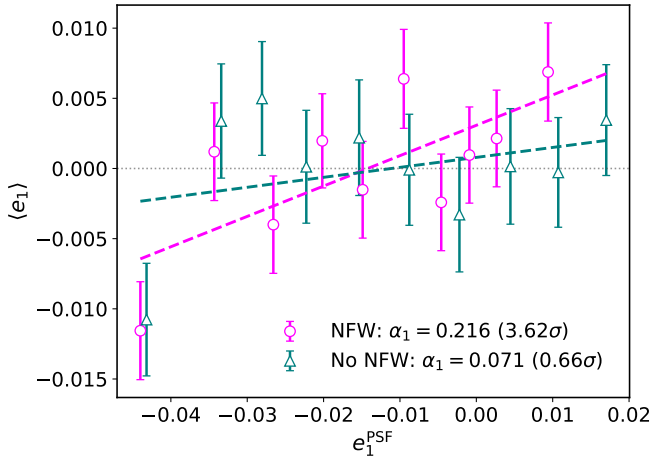


Figure 18. Test of PSF ellipticity leakage in simulations. Magenta points show results from fiducial simulations including NFW shear, while teal points show results from simulations without NFW shear. A significant correlation is observed only in the lensed case, indicating that the apparent signal arises from the lensing-induced shear geometry rather than from true PSF ellipticity leakage into galaxy shapes.

gion is indicated by the vertical grey shaded band in Figure 17. For the shear-bias estimation in the fiducial simulations, we also exclude objects for which the PSF ellipticity is large, i.e., $|e_i^{\text{PSF}}| > 0.05$. These objects are predominantly located near the edges of the field of view, where significant PSF ellipticity leakage is expected, as discussed in the following subsection. Within our gridded response calibration scheme, applying this PSF ellipticity cut significantly reduces the cross-shear signal in the outer regions of the profile, while leaving the estimated value of $\hat{\zeta}$ nearly unchanged.

5.4.3. PSF Ellipticity Leakage in Fiducial Simulations

As noted in the shape-catalog tests for real data (Section 4.5), we detect a significant correlation between PSF ellipticity and galaxy shapes in the e_1 component, suggestive of a possible PSF ellipticity leakage. We investigate this effect further using our fiducial simulations, which employ PSFEX PSF models derived from real data.

The fiducial simulations include lensing by an NFW cluster profile located at the centre of the field of view, closely mimicking the observational configuration of the real SuperBIT targets. To disentangle genuine PSF leakage from correlations induced by lensing geometry, we perform the same analysis on a control set of simulations that do not include any NFW shear, corresponding to an unlensed field with randomly oriented galaxies.

The results are shown in Figure 18. The fiducial simulations including NFW shear (magenta points) exhibit a

significant correlation, with a measured slope $\alpha_1 = 0.216$ at a 3.62σ significance. In contrast, simulations without NFW shear (teal points) show no statistically significant correlation, with $\alpha_1 = 0.071$ at a 0.66σ significance. For simulations without NFW shear, we also estimate the correlation between galaxy e_2 and e_2^{PSF} , obtaining $\alpha_2 = 0.059$ at 0.99σ significance. These results are obtained using objects for which the PSF ellipticity satisfies $|e| \leq 0.05$, corresponding to the dominant central region of the field of view.

However, the PSF becomes highly elliptical near the very edges of the field, where $|e| > 0.05$. When the leakage is evaluated including these regions in simulations without NFW shear, we detect a significant correlation, $\alpha_1 = 0.163$ at 4.15σ significance, indicating that PSF ellipticity leakage becomes important near the edges of the field. We note this as an avenue for future work, where we plan to investigate this effect using B -mode convergence maps, κ_B , and to mitigate it by excluding edge regions from science analyses.

These results indicate that the observed correlation in the fiducial simulations is not due to direct PSF ellipticity leakage into the galaxy shape measurements within the central field region. Instead, we interpret this effect as a geometric coincidence: the tangential shear pattern induced by the NFW lensing profile produces a spatial structure in $\langle e_1 \rangle$ that aligns with the CCD-coordinate pattern of e_1^{PSF} , thereby generating an apparent correlation without true PSF contamination in the central portion of the field of view.

6. CONCLUSION

We process imaging data obtained during SuperBIT’s 2023 flight and present shape catalogs for 30 science targets: primarily merging clusters and filamentary structures, together with 6 COSMOS fields observed mainly for calibration purposes. We obtain a mean density of selected objects of $n_{\text{sel}} = 14.16 \text{ arcmin}^{-2}$ and an average effective number density of $n_{\text{eff}}^{\text{H12}} = 11.04 \text{ arcmin}^{-2}$ across all targets. The full set of statistics for all fields is provided in Table 2.

The image processing and shape-measurement pipeline consists of multiple steps, including stacking of 36 single exposures, source extraction, masking of hot pixels, and removal of spurious detections associated with diffraction spikes around bright stars. Weak-lensing shapes are measured using the METACALIBRATION algorithm. We introduce a novel calibration technique based on a gridded shear-response defined in the two-dimensional space of METACALIBRATION quantities, together with galaxy weights constructed in this parameter space.

Two key requirements for precise weak-lensing shape measurements are: (1) accurate modeling of the PSF in the focal plane, and (2) forward modeling of that PSF for unbiased inference of galaxy shapes. To assess the robustness of both steps, we employ a comprehensive set of diagnostics. The PSF interpolation is validated using reserved test stars not used in PSF modeling, and the corresponding PSF residuals and ρ -statistics are computed to quantify the impact of PSF mis-modeling on the science analysis. To validate the shape measurements produced by the forward modeling with NGMIX, we investigate residual correlations between galaxy shapes, PSF properties, and METACALIBRATION quantities.

In parallel, we develop an image simulation pipeline to test the robustness of the full shape-measurement framework. The fiducial simulations use empirical SuperBIT PSFs obtained from PSFEX runs on real data in order to faithfully capture observational non-idealities. Validation is performed through a hierarchy of unit tests followed by fiducial simulations. Using a conventional global mean shear-response calibration, we find a tangential shear bias of $\sim 6.3\%$, which is reduced to 1.1% when employing the gridded shear-response calibration scheme. We further investigate PSF ellipticity leakage using the fiducial simulations and find no significant detection of true PSF-induced leakage.

This work forms part of the *Lensing in the Blue* series. Paper I & Paper II laid the foundations of the lensing analysis framework developed here, and the final convergence maps for the targets presented in this work (Paper III) will be reported in Paper IV. The important step of background–foreground separation using color information is not addressed in this paper and will be discussed in detail in Paper IV, together with an accompanying white paper describing the method.

At present, shapes are measured using only the primary science band F480W (*b*); a multi-band shape-measurement analysis is planned, and corresponding multi-band shape catalogs will be released in future data products. We also note that the current implementation of METACALIBRATION does not account for shear-dependent detection bias. We therefore plan to implement the METADETECTION framework (E. S. Sheldon et al. 2020) in future versions of the pipeline to mitigate this effect.

In the near future, SuperBIT’s merging cluster observations will be analyzed in multiple complementary frameworks, including analyses of offsets between X-ray emission, stellar mass, and dark matter distributions for SIDM constraints and an assessment of the dynamical states of SuperBIT clusters using the coherence of differ-

ent cluster components in Fourier space (G. Cerini et al. 2023).

SuperBIT’s three square degrees of high-resolution deep NUV and blue imaging adds legacy value to existing NASA data, and the object catalogs produced in this work can support a broad range of investigations beyond cluster cosmology. The three-band photometric data (F400W, F480W and F600W) are already being employed to study circumgalactic dust in the intracluster medium (A. Longobardi et al. 2020; J. E. McCleary et al. 2025). Photometric redshift estimation is another natural use case; the inclusion of near-ultraviolet photometry spanning the 3700 Å Balmer and 4000 Å Lyman breaks used in galaxy template fitting can halve uncertainties on photometric redshift estimates (M. Sawicki et al. 2019). Other potential use cases include searches for OB stars and white dwarfs, as well as studies of galaxy evolution.

ACKNOWLEDGMENTS

This work was completed primarily using the Explorer Cluster, supported by Northeastern University’s Research Computing team. Additional computations were performed by utilizing the CANDIDE cluster at the Institut d’Astrophysique de Paris, which was funded through grants from the PNCG, CNES, DIM-ACAV, and the Cosmic Dawn Center and maintained by Stephane Rouberol. SS thanks Dhayaa Anbajagane and Chihway Chang for useful discussions and feedback. SS also thanks Leila Ohashi and Marcus Michaud for creating star masks as part of the Young Scholars’ Program organized by Northeastern University. The development of analysis pipeline was partially supported by the Jet Propulsion Laboratory, California Institute of Technology, under a contract with the National Aeronautics and Space Administration (80NM0018D0004). The US team acknowledges support from the NASA APRA grant 80NSSC22K0365. Canadian team members acknowledge support from the Canadian Institute for Advanced Research (CIFAR), the Natural Science and Engineering Research Council (NSERC), and the Canadian Space Agency (CSA). UK coauthors acknowledge funding from Durham University’s Astronomy Projects Award, STFC (grants ST/P000541/1, ST/V005766/1 and ST/X001075/1), and UKRI (grant MR/X006069/1).

Based on data products from observations made with ESO Telescopes at the La Silla Paranal Observatory under ESO programme ID 179.A-2005 and on data products produced by TERAPIX and the Cambridge Astron-

omy Survey Unit on behalf of the UltraVISTA consortium.

This work has made use of data from the European Space Agency (ESA) mission *Gaia* (<https://www.cosmos.esa.int/gaia>), processed by the *Gaia* Data Processing and Analysis Consortium (DPAC, <https://www.cosmos.esa.int/web/gaia/dpac/consortium>). Funding for the DPAC has been provided by national institutions, in particular the institutions participating in the *Gaia* Multilateral Agreement.

The Pan-STARRS1 Surveys (PS1) and the PS1 public science archive have been made possible through contributions by the Institute for Astronomy, the University of Hawaii, the Pan-STARRS Project Office, the Max-Planck Society and its participating institutes, the Max Planck Institute for Astronomy, Heidelberg and the Max Planck Institute for Extraterrestrial Physics, Garching, The Johns Hopkins University, Durham University, the University of Edinburgh, the Queen’s University Belfast, the Harvard-Smithsonian Center for Astrophysics, the Las Cumbres Observatory Global Telescope Network Incorporated, the National Central University of Taiwan, the Space Telescope Science Institute, the National Aeronautics and Space Administration under Grant No. NNX08AR22G issued through the Planetary Science Division of the NASA Science Mission Directorate, the National Science Foundation Grant No. AST-1238877, the University of Maryland, Eotvos Lorand University (ELTE), the Los Alamos National Laboratory, and the Gordon and Betty Moore Foundation.

All the *Pan-STARRS1* data used in this paper can be found in MAST: [10.17909/s0zg-jx37](https://doi.org/10.17909/s0zg-jx37).

This paper is based on data collected at the Subaru Telescope and retrieved from the HSC data archive system, which is operated by the Subaru Telescope and Astronomy Data Center (ADC) at NAOJ. Data analysis was in part carried out with the cooperation of Center for Computational Astrophysics (CfCA), NAOJ. We are honored and grateful for the opportunity of observing the Universe from Maunakea, which has the cultural, historical and natural significance in Hawaii.

DATA AVAILABILITY

The imaging data, including the single exposures and coadded images, together with supplementary calibration products such as darks, flats, hot-pixel masks, and the photometric data catalogs, will soon be publicly available through the MAST archive ([10.17909/0hsg-dd76](https://doi.org/10.17909/0hsg-dd76)). The shape catalogs will be made publicly available following the publication of this paper and the convergence-map paper.

Software: Astropy (Astropy Collaboration et al. 2013, 2018, 2022), Swarp (E. Bertin 2010b) SEXTOR (E. Bertin & S. Arnouts 1996b), GalSim (B. Rowe et al. 2014), NGMIX (E. Sheldon 2015), NumPy (C. R. Harris et al. 2020), SciPy (P. Virtanen et al. 2020), HealPy (K. M. Górski et al. 2005; A. Zonca et al. 2019), Matplotlib (J. D. Hunter 2007)

APPENDIX

A. EXPOSURE QUALITY ASSESSMENT AND SELECTION

While all 300 s single exposures are used to construct deep coadded images for each SuperBIT target, additional care is required when selecting exposures for shape measurement. Accurate PSF deconvolution is essential for unbiased shape estimation with NGMIX, and we find that the quality of individual SuperBIT exposures can be highly inhomogeneous due to the unique observing conditions of the balloon-borne platform. This section is therefore dedicated to quantifying and selecting exposures suitable for shape measurement.

To assess exposure quality, we focus on two diagnostic criteria that we find to be most effective. The first is the scatter of the stellar locus in the size–magnitude diagram. The second is the mean ellipticity of point sources measured in the outer 50% area of the exposure. We find that the overall PSF ellipticity and stability of

PSF quality within an exposure is particularly sensitive to these two quantities.

Figure A1 illustrates the application of this exposure-selection scheme for the target Abell 3411. The upper panels show size–magnitude diagrams for two representative exposures: a “good” exposure with a compact, well-defined stellar locus (upper left) and a “bad” exposure with a more scattered stellar locus (upper right). In both panels, stars are color-coded by their distance from the center of the exposure. As shown, the increased size scatter is primarily associated with stars located near the outskirts of the exposure. The lower panels show the time evolution of the scatter in the PSF-star FWHM (middle panel) and the mean PSF ellipticity $\langle |e| \rangle = \sqrt{e_1^2 + e_2^2}$ measured in the outer regions of the CCD (lower panel) for all exposures of this target. The x-axis denotes the UTC time at which each exposure was taken.

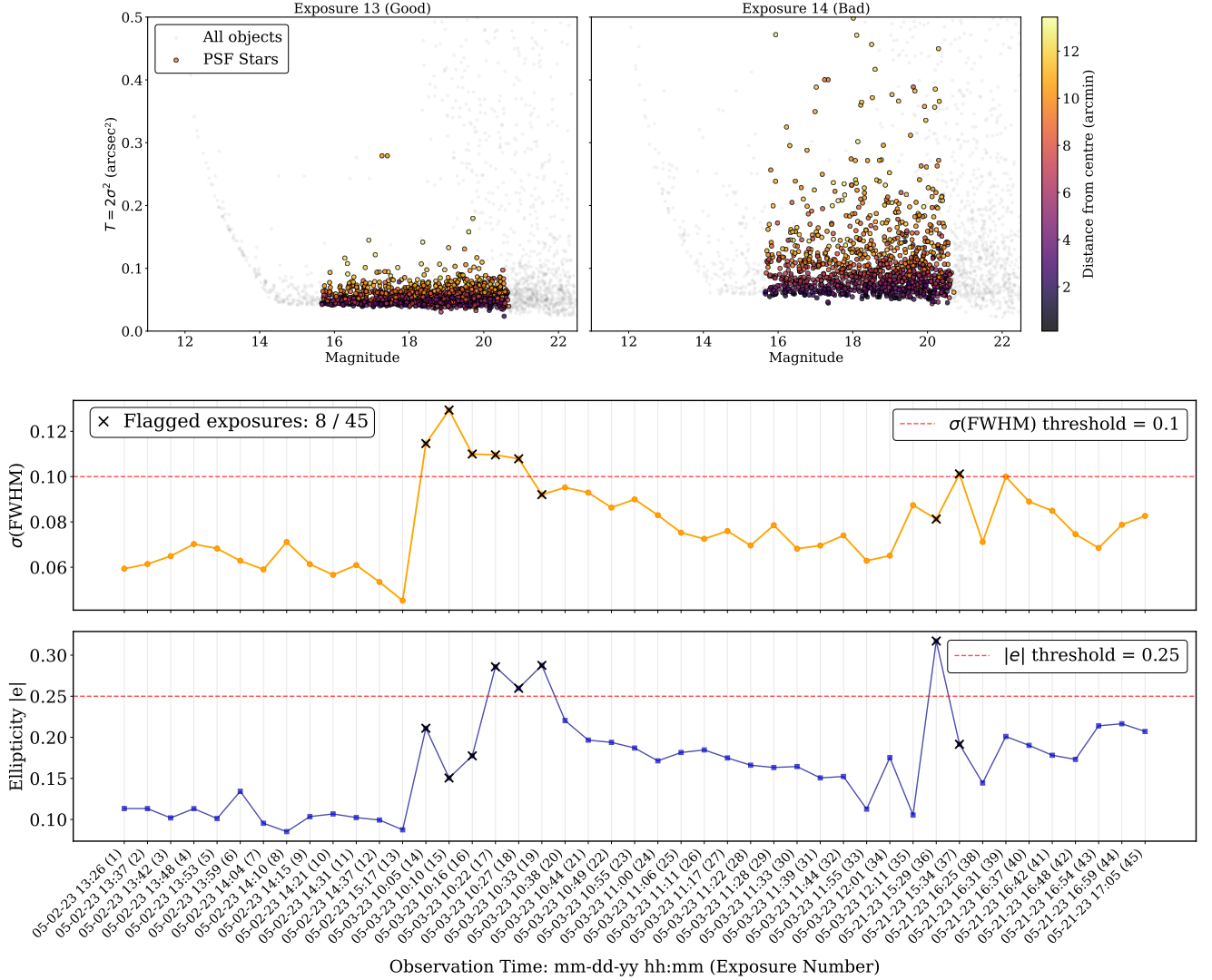


Figure A1. Illustration of the exposure-selection scheme used in our pipeline for the target Abell 3411. *Upper panels:* Size-magnitude diagrams for two representative exposures. The left panel shows a “good” exposure with a compact, well-defined stellar locus, while the right panel shows a “bad” exposure with a more scattered stellar locus. All detected objects are shown in gray, while the stars used for PSF modeling are highlighted with a colorbar, where the colorbar indicates the distance from the exposure center in arcminutes. The increased scatter in the stellar locus is primarily driven by stars located near the outskirts of the exposure. *Lower panels:* Temporal evolution of two exposure-quality diagnostics: the scatter of the PSF-star FWHM (middle panel) and the mean PSF ellipticity measured in the outer 50% of each exposure (bottom panel). The x-axis shows the UTC observation time together with the exposure number. Red dashed lines indicate the thresholds applied to each diagnostic. Exposures flagged by either criterion are marked with black crosses and are excluded from the shape-measurement analysis.

Exposures are flagged and excluded from the shape-measurement pipeline when either of the two selection criteria fails, namely $\sigma(\text{FWHM}) \geq 0.1$ or $\langle |e| \rangle \geq 0.25$. Flagged exposures are indicated by black crosses in Figure A1.

B. NGMIX SHAPE-MEASUREMENT WORKFLOW

In this appendix, we provide a brief overview of the NGMIX shape-measurement workflow used in our analysis. This description is intended to help readers who may

be using NGMIX for the first time understand how the algorithm operates within the SuperBIT pipeline. In addition, we evaluate the performance of the NGMIX PSF modeling in the context of SuperBIT observations, verifying that the Gaussian-mixture representation provides an adequate description of the PSF for our weak-lensing measurements.

NGMIX measures pre-PSF galaxy parameters for each object detected in the coadded image. Starting from the detection catalog in the coadd, we construct a Multi-

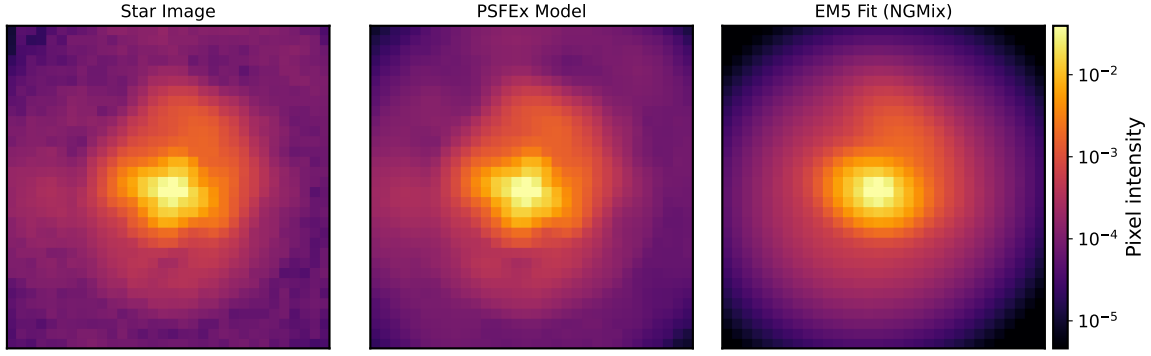


Figure B2. Downstream propagation of the PSF model through the pipeline. *Left:* normalized image of a test star as detected by the telescope. *Middle:* PSF model interpolated at the star position using PSFEX. *Right:* best-fit PSF model from NGMIX, represented by the `em5` Gaussian mixture model (a mixture of five Gaussians), which is used for Bayesian forward modeling in shape measurement. All images are displayed using a logarithmic color scale.

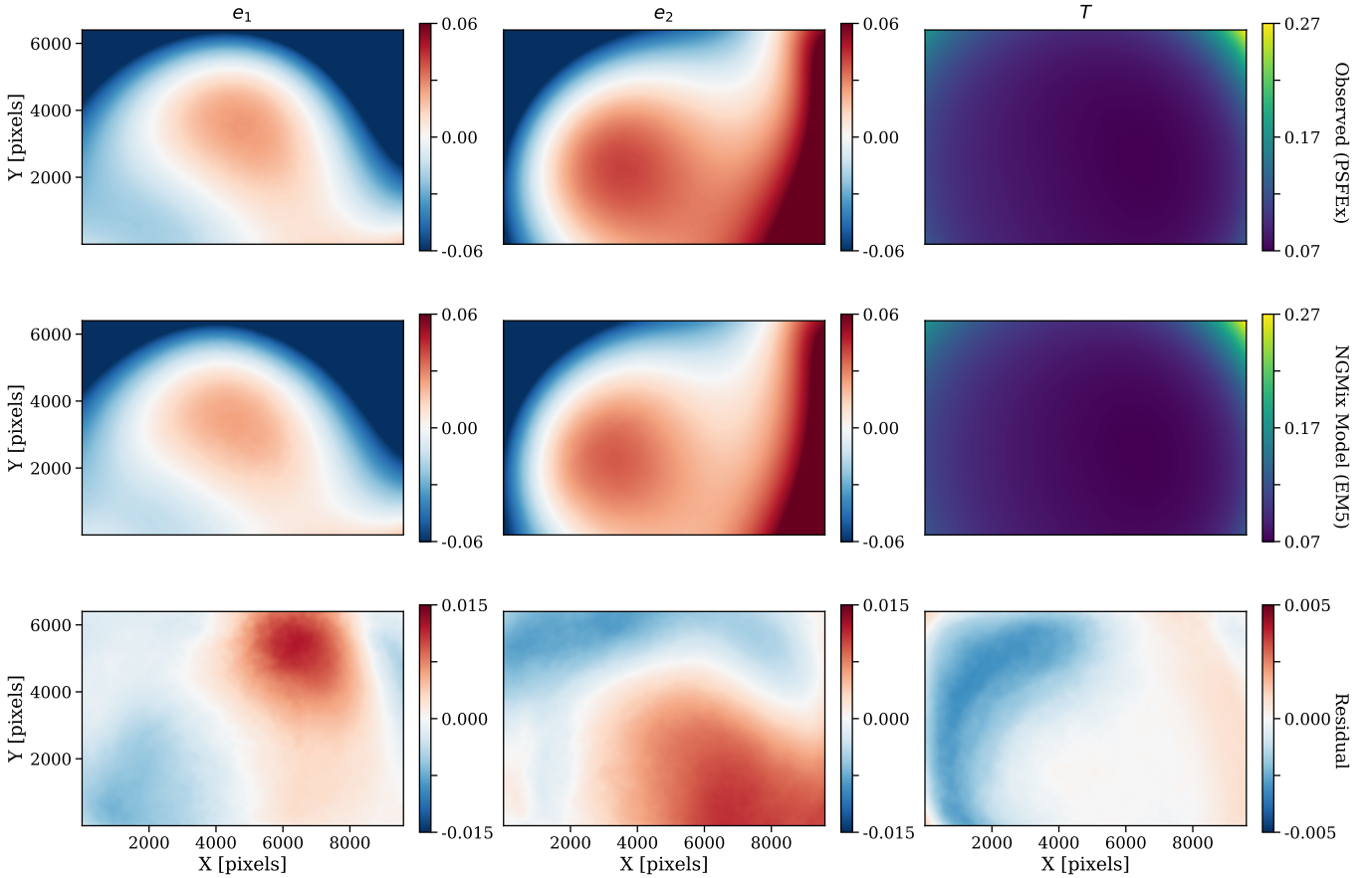


Figure B3. Evaluation of the ability of the NGMIX `em5` model to represent the SuperBIT PSF (here given by the PSFEX model). *Top panel:* PSF ellipticity components and size measured from the PSFEX model, rendered across the CCD coordinates of all exposures. *Middle panel:* Corresponding measurements from the best-fit NGMIX Gaussian-mixture model (`em5`). *Bottom panel:* Residuals between the PSFEX measurements and the best-fit `em5` model across the CCD.

Epoch Data Structure (MEDS)³⁷, which contains the image of each detected object in every exposure, the

corresponding PSF image, and the Jacobian of the WCS transformation for each exposure. The Jacobian encodes the orientation of the CCD plane at the time of each exposure, and due to telescope dithering, it differs be-

³⁷ <https://github.com/esheldon/meds/wiki>

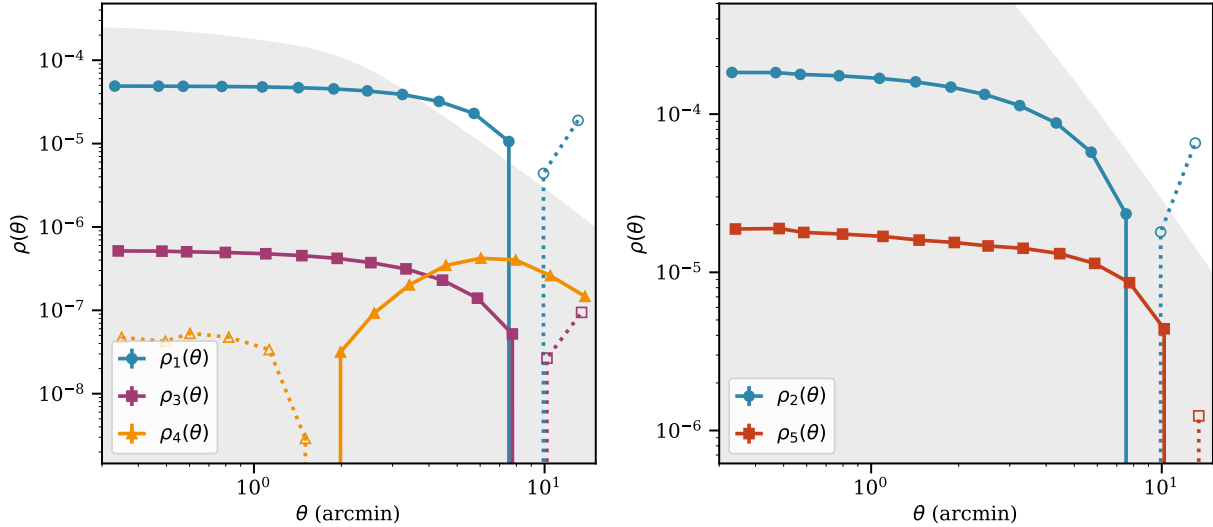


Figure B4. The ρ -statistics estimated from the ellipticity and size residuals of the best-fit **em5** model. The left panel shows ρ_1 , ρ_3 , and ρ_4 , while the right panel shows ρ_2 and ρ_5 . The gray shaded region in both panels corresponds to 10% of the expected two-point shear correlation signal for a representative SuperBIT galaxy cluster, computed using the same conservative assumptions described in Figure 10.

tween exposures; this is automatically accounted for in the MEDS-based shape measurement.

For each exposure, the observed galaxy image is formed by convolution of the intrinsic (pre-PSF) galaxy light profile with the SuperBIT PSF for that exposure, followed by pixelization and the addition of detector noise. Thus, for each galaxy we have a set of observed images $\{I^{\text{exp}}\}$ and corresponding PSF images $\{\text{PSF}^{\text{exp}}\}$ across the full exposure stack:

$$I_{i,j}^{\text{exp}} = (G \otimes \text{PSF}^{\text{exp}})_{i,j} + \eta_{i,j}^{\text{exp}}, \quad (\text{B1})$$

where (i, j) denote pixel coordinates in the two-dimensional cutouts, $\eta_{i,j}^{\text{exp}}$ is the detector noise for that exposure, and G is the pre-PSF galaxy model, assumed to be constant across all exposures.

The intrinsic galaxy model G is parametrized by the six parameters $\{c_x, c_y, e_1, e_2, f, T\}$, corresponding to the centroid coordinates (c_x, c_y) , ellipticity components (e_1, e_2) , flux f , and size T . While the galaxy parameters are constant across exposures, the PSF models and noise realizations vary between exposures.

The first step in NGMIX is a least-squares fit of a Gaussian mixture model to the PSF images. In our case, the **em5** model—a mixture of five Gaussians—is fitted to the PSF images, which are themselves interpolated models from PSFEX. This procedure yields best-fit PSF parameters for all $\{\text{PSF}^{\text{exp}}\}$ across the exposure stack. Figure B2 illustrates the downstream propagation of the PSF model through the pipeline, from the observed stellar image to the PSFEX interpolation and finally to the best-fit NGMIX Gaussian-mixture model

used for forward modeling. A key concern when using the NGMIX Gaussian-mixture representation is its ability to accurately capture the SuperBIT PSF. For ground-based telescopes, atmospheric seeing produces a relatively broad and smooth PSF that is well approximated by Gaussian mixtures. In contrast, for a balloon-borne mission such as SuperBIT, the absence of atmospheric seeing leads to a PSF with significant high-frequency structure (middle panel of Figure B2). These small-scale features are not fully captured by the best-fit **em5** Gaussian-mixture model (right panel), which smooths over much of the fine structure present in the PSFEX model. The key question is therefore whether this loss of high-frequency information introduces residual ellipticity in the PSF model that could bias weak-lensing measurements.

To assess this, we evaluate the ellipticity and size residuals between the PSFEX model rendered at the position of each galaxy and the best-fit **em5** Gaussian-mixture model of that rendering across the CCD. In Figure B3, the top row shows the spatial variation of the PSF ellipticity components (e_1, e_2) and size T measured from the PSFEX model, while the middle row shows the corresponding measurements from the best-fit **em5** model. The bottom row displays the residuals between the two as a function of CCD position. In Figure B4, we compute the ρ statistics of these residuals to quantify their potential impact on weak-lensing two-point correlation measurements, following the procedure described in Section 3. The shaded regions indicate the “safe zone,” defined as 10% of the expected shear two-

point correlation signal for a SuperBIT-like cluster given the anticipated background galaxy redshift distribution. All ρ statistics fall within this region, indicating that residual modeling errors from the `em5` representation are sufficiently small for the planned science analysis.

After fitting the PSF models, NGMIX performs a least-squares optimization of the posterior probability distribution for the galaxy model:

$$P(\theta_{\text{gal}} | \{I^{\text{exp}}\}) = \frac{\mathcal{L}(\{I^{\text{exp}}\} | G) P(G)}{P(\{I^{\text{exp}}\})}, \quad (\text{B2})$$

where \mathcal{L} is the likelihood and $P(G)$ is the prior on galaxy properties. The corresponding log-likelihood is given by

$$-2 \log \mathcal{L} = \sum_{\text{exp}} \sum_{i,j} \frac{[I_{i,j}^{\text{exp}} - (G \otimes \text{PSF}^{\text{exp}})_{i,j}]^2}{\sigma_{i,j}^2}. \quad (\text{B3})$$

REFERENCES

- Ade, P. A. R., et al. 2016, *Astron. Astrophys.*, 594, A24, doi: [10.1051/0004-6361/201525833](https://doi.org/10.1051/0004-6361/201525833)
- Aihara, H., et al. 2022, *Publ. Astron. Soc. Jap.*, 74, 247, doi: [10.1093/pasj/psab122](https://doi.org/10.1093/pasj/psab122)
- Allen, S. W., Evrard, A. E., & Mantz, A. B. 2011, *Ann. Rev. Astron. Astrophys.*, 49, 409, doi: [10.1146/annurev-astro-081710-102514](https://doi.org/10.1146/annurev-astro-081710-102514)
- Anbajagane, D., et al. 2025, *Open J. Astrophys.*, 8, 146158, doi: [10.33232/001c.146158](https://doi.org/10.33232/001c.146158)
- Andreon, S. 2016, *Astron. Astrophys.*, 587, A158, doi: [10.1051/0004-6361/201526852](https://doi.org/10.1051/0004-6361/201526852)
- Arnaud, M., Pointecouteau, E., & Pratt, G. W. 2005, *Astron. Astrophys.*, 441, 893, doi: [10.1051/0004-6361:20052856](https://doi.org/10.1051/0004-6361:20052856)
- Astropy Collaboration, Robitaille, T. P., Tollerud, E. J., et al. 2013, *A&A*, 558, A33, doi: [10.1051/0004-6361/201322068](https://doi.org/10.1051/0004-6361/201322068)
- Astropy Collaboration, Price-Whelan, A. M., Sipőcz, B. M., et al. 2018, *AJ*, 156, 123, doi: [10.3847/1538-3881/aabc4f](https://doi.org/10.3847/1538-3881/aabc4f)
- Astropy Collaboration, Price-Whelan, A. M., Lim, P. L., et al. 2022, *ApJ*, 935, 167, doi: [10.3847/1538-4357/ac7c74](https://doi.org/10.3847/1538-4357/ac7c74)
- Bacon, D. J., Refregier, A. R., & Ellis, R. S. 2000, *Mon. Not. Roy. Astron. Soc.*, 318, 625, doi: [10.1046/j.1365-8711.2000.03851.x](https://doi.org/10.1046/j.1365-8711.2000.03851.x)
- Bartelmann, M., & Schneider, P. 2001, *Phys. Rept.*, 340, 291, doi: [10.1016/S0370-1573\(00\)00082-X](https://doi.org/10.1016/S0370-1573(00)00082-X)
- Bernstein, G. M., & Jarvis, M. 2002, *Astron. J.*, 123, 583, doi: [10.1086/338085](https://doi.org/10.1086/338085)
- Bertin, E. 2010a, SWarp: Resampling and Co-adding FITS Images Together,, Astrophysics Source Code Library, record ascl:1010.068 <http://ascl.net/1010.068>
- Bertin, E. 2010b, SWarp: Resampling and Co-adding FITS Images Together,, Astrophysics Source Code Library, record ascl:1010.068 <http://ascl.net/1010.068>
- Bertin, E. 2011, in *Astronomical Society of the Pacific Conference Series*, Vol. 442, *Astronomical Data Analysis Software and Systems XX*, ed. I. N. Evans, A. Accomazzi, D. J. Mink, & A. H. Rots, 435
- Bertin, E., & Arnouts, S. 1996a, *A&AS*, 117, 393, doi: [10.1051/aas:1996164](https://doi.org/10.1051/aas:1996164)
- Bertin, E., & Arnouts, S. 1996b, *A&AS*, 117, 393, doi: [10.1051/aas:1996164](https://doi.org/10.1051/aas:1996164)
- Bridle, S., Balan, S. T., Bethge, M., et al. 2010, *MNRAS*, 405, 2044, doi: [10.1111/j.1365-2966.2010.16598.x](https://doi.org/10.1111/j.1365-2966.2010.16598.x)
- Casey, C. M., Kartaltepe, J. S., Drakos, N. E., et al. 2023, *ApJ*, 954, 31, doi: [10.3847/1538-4357/acc2bc](https://doi.org/10.3847/1538-4357/acc2bc)
- Cerini, G., Cappelluti, N., & Natarajan, P. 2023, *Astrophys. J.*, 945, 152, doi: [10.3847/1538-4357/acbccb](https://doi.org/10.3847/1538-4357/acbccb)
- Chambers, K. C., Magnier, E. A., Metcalfe, N., et al. 2016, arXiv e-prints, arXiv:1612.05560, doi: [10.48550/arXiv.1612.05560](https://doi.org/10.48550/arXiv.1612.05560)
- Clowe, D., Gonzalez, A., & Markevitch, M. 2004, *Astrophys. J.*, 604, 596, doi: [10.1086/381970](https://doi.org/10.1086/381970)
- DESI Collaboration, Abdul-Karim, M., Adame, A. G., et al. 2025, arXiv e-prints, arXiv:2503.14745, doi: [10.48550/arXiv.2503.14745](https://doi.org/10.48550/arXiv.2503.14745)
- Flewelling, H. A., Magnier, E. A., Chambers, K. C., et al. 2020, *ApJS*, 251, 7, doi: [10.3847/1538-4365/abb82d](https://doi.org/10.3847/1538-4365/abb82d)
- Fu, S., Dell'Antonio, I., Escalante, Z., et al. 2024, *ApJ*, 974, 69, doi: [10.3847/1538-4357/ad67c6](https://doi.org/10.3847/1538-4357/ad67c6)
- Gaia Collaboration. 2018, *A&A*, 616, A1, doi: [10.1051/0004-6361/201833051](https://doi.org/10.1051/0004-6361/201833051)

- Gaia Collaboration, Prusti, T., de Bruijne, J. H. J., et al. 2016, *A&A*, 595, A1, doi: [10.1051/0004-6361/201629272](https://doi.org/10.1051/0004-6361/201629272)
- Gaia Collaboration, Vallenari, A., Brown, A. G. A., et al. 2023, *A&A*, 674, A1, doi: [10.1051/0004-6361/202243940](https://doi.org/10.1051/0004-6361/202243940)
- Gatti, M., et al. 2021, *Mon. Not. Roy. Astron. Soc.*, 504, 4312, doi: [10.1093/mnras/stab918](https://doi.org/10.1093/mnras/stab918)
- Gill, A., Benton, S. J., Brown, A. M., et al. 2020, *AJ*, 160, 266, doi: [10.3847/1538-3881/abbffb](https://doi.org/10.3847/1538-3881/abbffb)
- Gill, A. S., et al. 2022, *Proc. SPIE Int. Soc. Opt. Eng.*, 12191, 1219114, doi: [10.1117/12.2627564](https://doi.org/10.1117/12.2627564)
- Gill, A. S., Benton, S. J., Damaren, C. J., et al. 2024, *Astron. J.*, 168, 85, doi: [10.3847/1538-3881/ad5840](https://doi.org/10.3847/1538-3881/ad5840)
- Górski, K. M., Hivon, E., Banday, A. J., et al. 2005, *ApJ*, 622, 759, doi: [10.1086/427976](https://doi.org/10.1086/427976)
- Harris, C. R., Millman, K. J., van der Walt, S. J., et al. 2020, *Nature*, 585, 357, doi: [10.1038/s41586-020-2649-2](https://doi.org/10.1038/s41586-020-2649-2)
- Harvey, D., Massey, R., Kitching, T., Taylor, A., & Tittley, E. 2015, *Science*, 347, 1462, doi: [10.1126/science.1261381](https://doi.org/10.1126/science.1261381)
- Harvey, D., Robertson, A., Massey, R., & Kneib, J.-P. 2017, *MNRAS*, 464, 3991, doi: [10.1093/mnras/stw2671](https://doi.org/10.1093/mnras/stw2671)
- Heymans, C., et al. 2006, *Mon. Not. Roy. Astron. Soc.*, 368, 1323, doi: [10.1111/j.1365-2966.2006.10198.x](https://doi.org/10.1111/j.1365-2966.2006.10198.x)
- Heymans, C., Van Waerbeke, L., Miller, L., et al. 2012, *MNRAS*, 427, 146, doi: [10.1111/j.1365-2966.2012.21952.x](https://doi.org/10.1111/j.1365-2966.2012.21952.x)
- Hirata, C. M., & Seljak, U. 2003, *Mon. Not. Roy. Astron. Soc.*, 343, 459, doi: [10.1046/j.1365-8711.2003.06683.x](https://doi.org/10.1046/j.1365-8711.2003.06683.x)
- Huff, E., & Mandelbaum, R. 2017, <https://arxiv.org/abs/1702.02600>
- Hunter, J. D. 2007, *Computing in Science & Engineering*, 9, 90, doi: [10.1109/MCSE.2007.55](https://doi.org/10.1109/MCSE.2007.55)
- Jarvis, M., Bernstein, G., & Jain, B. 2004, *Mon. Not. Roy. Astron. Soc.*, 352, 338, doi: [10.1111/j.1365-2966.2004.07926.x](https://doi.org/10.1111/j.1365-2966.2004.07926.x)
- Jarvis, M., Bernstein, G. M., Fischer, P., et al. 2003, *Astron. J.*, 125, 1014, doi: [10.1086/367799](https://doi.org/10.1086/367799)
- Jarvis, M., et al. 2016, *Mon. Not. Roy. Astron. Soc.*, 460, 2245, doi: [10.1093/mnras/stw990](https://doi.org/10.1093/mnras/stw990)
- Joye, W. A., & Mandel, E. 2003, in *Astronomical Society of the Pacific Conference Series*, Vol. 295, *Astronomical Data Analysis Software and Systems XII*, ed. H. E. Payne, R. I. Jedrzejewski, & R. N. Hook, 489
- Kaiser, N., & Squires, G. 1993, *ApJ*, 404, 441, doi: [10.1086/172297](https://doi.org/10.1086/172297)
- Kaiser, N., Wilson, G., & Luppino, G. A. 2000, *Large-Scale Cosmic Shear Measurements*, <https://arxiv.org/abs/astro-ph/0003338>
- Kitching, T. D., Balan, S. T., Bridle, S., et al. 2012, *MNRAS*, 423, 3163, doi: [10.1111/j.1365-2966.2012.21095.x](https://doi.org/10.1111/j.1365-2966.2012.21095.x)
- Koester, B. P., McKay, T. A., Annis, J., et al. 2007, *Astrophys. J.*, 660, 221, doi: [10.1086/512092](https://doi.org/10.1086/512092)
- Laigle, C., McCracken, H. J., et al. 2021, *COSMOS2015 Catalog*, IPAC, doi: [10.26131/IRSA527](https://doi.org/10.26131/IRSA527)
- Laigle, C., et al. 2016, *Astrophys. J. Suppl.*, 224, 24, doi: [10.3847/0067-0049/224/2/24](https://doi.org/10.3847/0067-0049/224/2/24)
- Lang, D., Hogg, D. W., Mierle, K., Blanton, M., & Roweis, S. 2010, *AJ*, 139, 1782, doi: [10.1088/0004-6256/139/5/1782](https://doi.org/10.1088/0004-6256/139/5/1782)
- Leauthaud, A., Massey, R., Kneib, J.-P., et al. 2007, *ApJS*, 172, 219, doi: [10.1086/516598](https://doi.org/10.1086/516598)
- Lewis, A. 2025, *JCAP*, 08, 025, doi: [10.1088/1475-7516/2025/08/025](https://doi.org/10.1088/1475-7516/2025/08/025)
- Li, X., Li, Y., & Massey, R. 2022, *Monthly Notices of the Royal Astronomical Society*, 511, 4850–4860, doi: [10.1093/mnras/stac342](https://doi.org/10.1093/mnras/stac342)
- Li, X., & Mandelbaum, R. 2023, *Mon. Not. Roy. Astron. Soc.*, 521, 4904, doi: [10.1093/mnras/stad890](https://doi.org/10.1093/mnras/stad890)
- Longobardi, A., Boselli, A., Boissier, S., et al. 2020, *A&A*, 633, L7, doi: [10.1051/0004-6361/201937024](https://doi.org/10.1051/0004-6361/201937024)
- MacCrann, N., et al. 2021, *Mon. Not. Roy. Astron. Soc.*, 509, 3371, doi: [10.1093/mnras/stab2870](https://doi.org/10.1093/mnras/stab2870)
- Mandelbaum, R. 2018, *Ann. Rev. Astron. Astrophys.*, 56, 393, doi: [10.1146/annurev-astro-081817-051928](https://doi.org/10.1146/annurev-astro-081817-051928)
- Mandelbaum, R., Hirata, C. M., Seljak, U., et al. 2005, *Mon. Not. Roy. Astron. Soc.*, 361, 1287, doi: [10.1111/j.1365-2966.2005.09282.x](https://doi.org/10.1111/j.1365-2966.2005.09282.x)
- Mandelbaum, R., et al. 2015, *Mon. Not. Roy. Astron. Soc.*, 450, 2963, doi: [10.1093/mnras/stv781](https://doi.org/10.1093/mnras/stv781)
- Mantz, A. B., Allen, S. W., Morris, R. G., et al. 2014, *Mon. Not. Roy. Astron. Soc.*, 440, 2077, doi: [10.1093/mnras/stu368](https://doi.org/10.1093/mnras/stu368)
- Mantz, A. B., et al. 2015, *Mon. Not. Roy. Astron. Soc.*, 446, 2205, doi: [10.1093/mnras/stu2096](https://doi.org/10.1093/mnras/stu2096)
- Massey, R., Kitching, T., & Nagai, D. 2011, *MNRAS*, 413, 1709, doi: [10.1111/j.1365-2966.2011.18246.x](https://doi.org/10.1111/j.1365-2966.2011.18246.x)
- Massey, R., Heymans, C., Bergé, J., et al. 2007, *Monthly Notices of the Royal Astronomical Society*, 376, 13–38, doi: [10.1111/j.1365-2966.2006.11315.x](https://doi.org/10.1111/j.1365-2966.2006.11315.x)
- McCleary, J. E., Huff, E. M., Bartlett, J. W., & Hensley, B. S. 2025, <https://arxiv.org/abs/2503.04098>
- McCleary, J. E., Everett, S. W., Shaaban, M. M., et al. 2023, *Astron. J.*, 166, 134, doi: [10.3847/1538-3881/ace7ca](https://doi.org/10.3847/1538-3881/ace7ca)
- Paracha, E., Benton, S. J., Damaren, C. J., et al. 2024, in *Proc. SPIE*, doi: [10.1117/12.3019360](https://doi.org/10.1117/12.3019360)
- Prat, J., Blazek, J., Sánchez, C., et al. 2022, *PhRvD*, 105, 083528, doi: [10.1103/PhysRevD.105.083528](https://doi.org/10.1103/PhysRevD.105.083528)
- Randall, S. W., Markevitch, M., Clowe, D., Gonzalez, A. H., & Bradač, M. 2008, *ApJ*, 679, 1173, doi: [10.1086/587859](https://doi.org/10.1086/587859)

- Robertson, A., Massey, R., & Eke, V. 2017, *Mon. Not. Roy. Astron. Soc.*, 465, 569, doi: [10.1093/mnras/stw2670](https://doi.org/10.1093/mnras/stw2670)
- Romualdez, L. J., Benton, S. J., Brown, A. M., et al. 2020, *Rev. Sci. Instrum.*, 91, 034501, doi: [10.1063/1.5139711](https://doi.org/10.1063/1.5139711)
- Rowe, B. 2010, *MNRAS*, 404, 350, doi: [10.1111/j.1365-2966.2010.16277.x](https://doi.org/10.1111/j.1365-2966.2010.16277.x)
- Rowe, B., et al. 2014, <https://arxiv.org/abs/1407.7676>
- Sawicki, M., Arnouts, S., Huang, J., et al. 2019, *Monthly Notices of the Royal Astronomical Society*, 489, 5202
- Schneider, P. 2006, in 33rd Advanced Saas Fee Course on Gravitational Lensing: Strong, Weak, and Micro, 269–451, doi: [10.1007/978-3-540-30310-7_3](https://doi.org/10.1007/978-3-540-30310-7_3)
- Schneider, P., & Seitz, C. 1995, *Astron. Astrophys.*, 294, 411. <https://arxiv.org/abs/astro-ph/9407032>
- Scoville, N., Abraham, R. G., Aussel, H., et al. 2007, *ApJS*, 172, 38, doi: [10.1086/516580](https://doi.org/10.1086/516580)
- Shaaban, M. M., Gill, A. S., McCleary, J., et al. 2022, *AJ*, 164, 245, doi: [10.3847/1538-3881/ac9b1c](https://doi.org/10.3847/1538-3881/ac9b1c)
- Sheldon, E. 2015, NGMIX: Gaussian mixture models for 2D images, *Astrophysics Source Code Library*, record ascl:1508.008 <http://ascl.net/1508.008>
- Sheldon, E. S. 2014, *Mon. Not. Roy. Astron. Soc.*, 444, 25, doi: [10.1093/mnrasl/slu104](https://doi.org/10.1093/mnrasl/slu104)
- Sheldon, E. S., Becker, M. R., MacCrann, N., & Jarvis, M. 2020, *Astrophys. J.*, 902, 138, doi: [10.3847/1538-4357/abb595](https://doi.org/10.3847/1538-4357/abb595)
- Sheldon, E. S., & Huff, E. M. 2017, *Astrophys. J.*, 841, 24, doi: [10.3847/1538-4357/aa704b](https://doi.org/10.3847/1538-4357/aa704b)
- Sirks, E. L., Clark, P., Massey, R. J., et al. 2020, *J. of Instrum.*, 15, P05014, doi: [10.1088/1748-0221/15/05/P05014](https://doi.org/10.1088/1748-0221/15/05/P05014)
- Sirks, E. L., Harvey, D., Massey, R., et al. 2024, *Mon. Not. Roy. Astron. Soc.*, 530, 3160, doi: [10.1093/mnras/stae1012](https://doi.org/10.1093/mnras/stae1012)
- van Dokkum, P. G. 2001, *PASP*, 113, 1420, doi: [10.1086/323894](https://doi.org/10.1086/323894)
- Van Waerbeke, L., Mellier, Y., Erben, T., et al. 2000, *A&A*, 358, 30, doi: [10.48550/arXiv.astro-ph/0002500](https://doi.org/10.48550/arXiv.astro-ph/0002500)
- Vanderlinde, K., et al. 2010, *Astrophys. J.*, 722, 1180, doi: [10.1088/0004-637X/722/2/1180](https://doi.org/10.1088/0004-637X/722/2/1180)
- Vikhlinin, A., et al. 2009, *Astrophys. J.*, 692, 1060, doi: [10.1088/0004-637X/692/2/1060](https://doi.org/10.1088/0004-637X/692/2/1060)
- Virtanen, P., Gommers, R., Oliphant, T. E., et al. 2020, *Nature Methods*, 17, 261, doi: [10.1038/s41592-019-0686-2](https://doi.org/10.1038/s41592-019-0686-2)
- Voyer, P., Benton, S. J., Damaren, C. J., et al. 2024, in *Proc. SPIE*, doi: [10.1117/12.3017869](https://doi.org/10.1117/12.3017869)
- Wittman, D., Golovich, N., & Dawson, W. A. 2018, *ApJ*, 869, 104, doi: [10.3847/1538-4357/aace77](https://doi.org/10.3847/1538-4357/aace77)
- Wittman, D. M., Tyson, J. A., Kirkman, D., Dell’Antonio, I., & Bernstein, G. 2000, *Nature*, 405, 143, doi: [10.1038/35012001](https://doi.org/10.1038/35012001)
- Yamamoto, M., et al. 2025, <https://arxiv.org/abs/2501.05665>
- Zenteno, A., Hernández-Lang, D., Klein, M., et al. 2020, *Monthly Notices of the Royal Astronomical Society*, 495, 705, doi: [10.1093/mnras/staa1157](https://doi.org/10.1093/mnras/staa1157)
- Zonca, A., Singer, L., Lenz, D., et al. 2019, *Journal of Open Source Software*, 4, 1298, doi: [10.21105/joss.01298](https://doi.org/10.21105/joss.01298)
- Zuntz, J., et al. 2018, *Mon. Not. Roy. Astron. Soc.*, 481, 1149, doi: [10.1093/mnras/sty2219](https://doi.org/10.1093/mnras/sty2219)